Competing quantum paramagnetic ground states of the Heisenberg antiferromagnet on the star lattice

Bohm-Jung Yang,[1] Arun Paramekanti,[1] and Yong Baek Kim[1,2]
[1]*Department of Physics, University of Toronto, Toronto, Ontario, Canada M5S 1A7*
[2]*School of Physics, Korea Institute for Advanced Study, Seoul 130-722, Korea*
(Received 1 December 2009; published 15 April 2010)

We investigate various competing paramagnetic ground states of the Heisenberg antiferromagnet on the two-dimensional star lattice which exhibits geometric frustration. Using slave particle mean-field theory combined with a projective symmetry group analysis, we examine a variety of candidate spin liquid states on this lattice, including chiral spin liquids, spin liquids with Fermi surfaces of spinons, and nematic spin liquids which break lattice rotational symmetry. Motivated by connection to large-N SU(N) theory as well as numerical exact diagonalization studies, we also examine various valence-bond solid (VBS) states on this lattice. Based on a study of energetics using Gutzwiller projected states, we find that a fully gapped spin liquid state is the lowest-energy spin liquid candidate for this model. We also find from a study of energetics using Gutzwiller projected wave functions and bond operator approaches that this spin liquid is unstable toward two different VBS states—a VBS state which respects all the Hamiltonian symmetries and a VBS state which exhibits $\sqrt{3}\times\sqrt{3}$ order—depending on the ratio of the Heisenberg exchange couplings on the two inequivalent bonds of the lattice. We compute the triplon dispersion in both VBS states within the bond operator approach and discuss possible implications of our work for future experiments on candidate materials.

DOI: 10.1103/PhysRevB.81.134418 PACS number(s): 74.20.Mn, 74.25.Dw

I. INTRODUCTION

In recent years, several geometrically frustrated spin-1/2 magnets have been synthesized which appear to not order magnetically even at temperatures well below the characteristic exchange couplings. Among these are the quasi-two-dimensional (2D) triangular organic material κ-BEDT(CN)$_3$,[1] the kagome lattice herbertsmithite[2] and distorted kagome lattice volborthite,[3] and the three-dimensional hyperkagome lattice magnet[4] $Na_4Ir_3O_8$. A large class of these magnets appear to exhibit gapless spin liquid behavior down to very low temperatures, leading to the exciting possibility that they may possess exotic ground states with fractionalized excitations.[5–13] Others among these have been proposed to weakly order into singlet valence-bond solid (VBS) states which break lattice symmetries.[14–17] As yet, there is no clear picture of what combination of geometric effects and spin interactions will lead to spin liquid ground states or VBS ground states; this necessitates a theoretical and experimental exploration of various new lattice geometries as well as possible ring-exchange interactions beyond the simplest Heisenberg spin-exchange interaction.

In this paper, we focus on understanding several competing ground states of the nearest-neighbor $S=1/2$ Heisenberg model

$$H=\sum_{\langle i,j\rangle} J_{i,j}\mathbf{S}_i\cdot\mathbf{S}_j, \tag{1}$$

on the 2D star lattice, shown in Fig. 1, as a function of J_t/J_e where J_t and J_e are the exchange couplings on the "triangle bonds" and "expanded bonds." Our motivation for this paper is twofold. First, the recent synthesis of a "star lattice" organic iron acetate quantum magnet[18] raises the possibility that a $S=1/2$ variant may possibly be synthesized in the near future and our results should be applicable to such systems. Second, this lattice has a sufficiently different geometry from more commonly studied quantum magnets—it may be viewed either as a variant of the kagome lattice or as a decorated honeycomb lattice—which allows us to explore the ef-

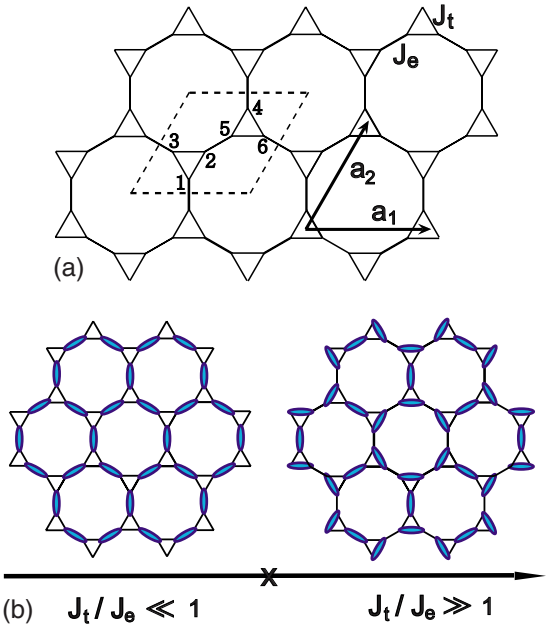

FIG. 1. (Color online) Top: structure of the star lattice depicting the six-site unit cell, the chosen lattice basis vectors $\mathbf{a}_1=2\hat{\mathbf{x}}$ and $\mathbf{a}_2=\hat{\mathbf{x}}+\sqrt{3}\hat{\mathbf{y}}$, and the bonds with Heisenberg exchange couplings J_e (expanded bonds) and J_t (triangle bonds). Bottom: phase diagram of the antiferromagnetic Heisenberg model on the star lattice. For $J_t/J_e\ll 1$, the ground state is a valence-bond solid (VBS) phase (J_e-dimer VBS) in which every dimer sits on the expanded links connecting neighboring triangles. For $J_t/J_e\gg 1$, the ground state is a VBS with an 18-site unit cell (the columnar 18-site VBS).

fect of this lattice geometry on possible spin liquid physics and valence-bond solid phases in quasi-2D systems. Recent studies of various model Hamiltonians on the star lattice[19–21] demonstrate that quantum phases on the star lattice have unique characteristics distinct from the properties of the phases on the honeycomb or kagome lattices.

Motivated by interpolating between this spin-1/2 SU(2) model and an SU(N) generalization at large N which permits a mean-field solution with fermionic spinon excitations,[22–24] we examine a large number of interesting U(1) spin liquids as candidate ground states of the nearest-neighbor $S=1/2$ Heisenberg model on the 2D star lattice. Guided by earlier work on the kagome lattice,[9] we focus on spin liquid states denoted by $\mathrm{SL}[\Phi_{\triangle},\Phi_{\nabla},\Phi_{dodecagon}]$ where $\Phi_{\triangle}$, Φ_{∇}, and $\Phi_{dodecagon}$ denote, respectively, the "fictitious" fluxes seen by the fermionic spinons as they move around an elementary plaquette of the lattice: an up triangular plaquette $\triangle$, a down triangular plaquette ∇, or the 12-site dodecagon plaquette. In terms of the original spin variable, the fluxes on the triangular plaquettes correspond to scalar spin chiralities of the form $\mathbf{S}_1\cdot\mathbf{S}_2\times\mathbf{S}_3$, while $\Phi_{dodecagon}$ is related to an operator defined by the 12 spins around the dodecagon loop. Depending on the flux values, these spin liquids represent gapped chiral spin liquids which break time-reversal symmetry[25] or states with gapless Fermi surfaces of spinons or gapped spin liquids with no broken symmetries.

From a study of energetics of various flux values using Gutzwiller projected wave-function numerics for the physical case of $N=2$, we show that a particular gapped spin liquid, which we denote as $\mathrm{SL}[0,0,\pi]$, which does not break lattice or time-reversal symmetries emerges as a favorable candidate over a wide range of J_t/J_e. This is in striking contrast to earlier work on the kagome lattice from two perspectives. First, as we show, the effect of projection is far more dramatic on the star lattice when compared with the kagome lattice; a numerical Gutzwiller projection of the mean-field states leads to a complete reordering of the energies of the candidate spin liquids. Second, unlike the kagome lattice case where the lowest-energy variational state of this form is a spin liquid with massless Dirac fermion excitations,[9] the $\mathrm{SL}[0,0,\pi]$ is a gapped U(1) spin liquid—we therefore know that it is ultimately unstable toward spinon confinement at low energies[26] unlike the Dirac fermion states whose stability depends on the number of fermion flavors N.[27]

We find that the $\mathrm{SL}[0,0,\pi]$ state naturally forms strong dimers on the expanded bonds for small values of J_t/J_e thus leading to a confined state, a J_e- dimer VBS, which respects all symmetries of the Hamiltonian.[28] For large J_t/J_e, numerical exact diagonalization (ED) studies of this model carried out in a restricted nearest-neighbor dimer basis showed signatures of $\sqrt{3}\times\sqrt{3}$ ordering.[29] We argue that another motivation to study possible dimer orders that break lattice symmetries is that such ordering often appear quite naturally in the large-N fermionic SU(N) theory as recognized in the early work of Affleck and Marston[14,23] and shown in various other models studied recently.[30–32] Inspired by these results, we consider various candidate VBS phases from different perspectives—a large-N route, a bond operator formalism, and Gutzwiller projected wave-function numerics. All of these points to a transition to a $\sqrt{3}\times\sqrt{3}$ ordered VBS phase for large enough $J_t/J_e\gtrsim 2-2.5$, leading us to the phase diagram shown in Fig. 1. Our result is in broad agreement with the ED study although the transition point estimated from our work is somewhat larger than the ED result which yields $(J_t/J_e)_{\mathrm{crit}}\approx 1.3$; the ED result may, however, may suffer from significant finite-size effects. We then discuss possible routes by which the $\mathrm{SL}[0,0,\pi]$ state might be unstable toward such $\sqrt{3}\times\sqrt{3}$ VBS order instead of the J_e-dimer VBS. We present results for the triplon dispersion in both VBS states which can be tested in inelastic neutron-scattering experiments on candidate materials.

Finally, although the various other interesting spin liquids we study do not appear to be energetically viable ground states for the nearest-neighbor Heisenberg model on the star lattice, they have energies which are close to the ground state. They might thus be stabilized as ground states by small changes in the Hamiltonian, such as further neighbor exchange or spin-phonon coupling or they might be relevant to understanding the intermediate energy scale properties or finite temperature physics of materials which realize this model. We therefore elucidate some of the properties of these spin liquid states.

This paper is organized as follows. We begin, in Sec. II by formulating the mean-field theory of the Heisenberg model on this lattice in a slave particle description using fermionic spinons which we relate to a large-N SU(N) approach. Based on this, we classify and study the physical properties of a number of candidate spin liquid Ansätze. We next turn, in Sec. III, to a study of dimerized states on this lattice and present a group theoretic classification of $\sqrt{3}\times\sqrt{3}$ orders as well as a large-N justification of specific candidate VBS phases. Section IV contains a discussion of the energetics of various spin liquid states using mean-field theory as well as a Gutzwiller projected wave-function study and bond operator approaches of candidate VBS phases. Section V discusses the various ways in which the $\mathrm{SL}[0,0,\pi]$ state, which is the lowest-energy spin liquid state, might be unstable toward VBS ordering as a result of spinon interactions and from a Gutzwiller wave-function approach. The phase transition between VBS phases is described in Sec. VI. Section VII contains a discussion of the triplon dispersion in both VBS states which we think are realized in this model. We conclude with a discussion about experimental implications in Sec. VIII. Details of various calculations are contained in Appendixes A and C.

II. SPIN LIQUID PHASES ON THE STAR LATTICE

A. Formulation of the mean-field theory

We investigate the ground state of the nearest-neighbor $S=1/2$ Heisenberg antiferromagnet on the star lattice, which is described in Eq. (1). Natural description of this lattice system requires the consideration of two inequivalent links, that is, one link lying on a triangle (a triangular link) and the other link connecting two neighboring triangles (an expanded link). We assign two different exchange couplings J_e and J_t on expanded and triangular links, respectively. We can also label a site i by pairs $(\mathbf{R},n)$, where $\mathbf{R}$ denotes the loca-

tion of a unit cell and n labels the six sites inside a single unit cell (see Fig. 1).

To construct spin liquid states we introduce the fermionic spinon operators, f_σ ($\sigma=\uparrow$ *or* $\downarrow$) to represent the spin operator;

$$S_i^\alpha = \frac{1}{2}\sum_{\sigma_1,\sigma_2} f_{i,\sigma_1}^\dagger \sigma_{\sigma_1,\sigma_2}^\alpha f_{i,\sigma_2}, \quad (\alpha = x,y,z). \tag{2}$$

Since this representation alone contains unphysical local configurations enlarging the Hilbert space, we have to impose the following local constraint, $f_\uparrow^\dagger f_\uparrow + f_\downarrow^\dagger f_\downarrow = 1$, to recover the physical Hilbert space. Using the fermionic spinon representation of the spin operator, the Heisenberg spin Hamiltonian can be rewritten as follows:

$$H = -\sum_{\sigma_1,\sigma_2}\sum_{\langle ij\rangle} \frac{J_{ij}}{2} f_{i,\sigma_1}^\dagger f_{j,\sigma_1} f_{j,\sigma_2}^\dagger f_{i,\sigma_2}. \tag{3}$$

Here we have dropped unimportant constant terms.

To decouple the four fermion interaction term we define spin singlet order parameters, $\chi_{ij} \equiv \frac{1}{2}\Sigma_\sigma \langle f_{i,\sigma}^\dagger f_{j,\sigma}\rangle$. After imposing the single occupancy constraint using the Lagrange multipliers μ_i, the mean-field Hamiltonian is given by

$$H_{MF} = -\sum_\sigma \sum_{\langle ij\rangle} J_{ij}(f_{i,\sigma}^\dagger f_{j,\sigma}\chi_{ij}^* + \text{H.c.}) + \sum_{\langle ij\rangle} 2J_{ij}|\chi_{ij}|^2 + \sum_{i,\sigma} \mu_i (f_{i,\sigma}^\dagger f_{i,\sigma} - 1). \tag{4}$$

To describe the phase fluctuation of the mean-field Ansatz, we express χ_{ij} as $\chi_{ij} = \bar{\chi}_{ij}\, e^{ia_{ij}}$, which leads to the following Hamiltonian:

$$H_{\mathrm{U}(1)} = -\sum_\sigma \sum_{\langle ij\rangle} J_{ij}(f_{i,\sigma}^\dagger f_{j,\sigma}\bar{\chi}_{ij} e^{-ia_{ij}} + \text{H.c.}) + \sum_{i,\sigma} \mu_i (f_{i,\sigma}^\dagger f_{i,\sigma} - 1). \tag{5}$$

In the above Hamiltonian $H_{\mathrm{U}(1)}$, the local U(1) gauge symmetry of the spin Hamiltonian which comes from the local conservation of the fermion number is manifest via the following gauge transformation:[33,34]

$$f_i \to f_i e^{i\theta_i},$$

$$a_{ij} \to a_{ij} - \theta_i + \theta_j. \tag{6}$$

Here a_{ij} describing the phase fluctuation of χ_{ij} plays the role of the spatial components of the U(1) gauge field. Namely, we have reformulated the quantum spin model as the problem of the spinons strongly coupled to the U(1) gauge field.

A systematic way of studying the coupled spinon and gauge field system is to consider the large-N reformulation of the problem extending the spin SU(2) symmetry to SU(N) (with N even).[23,24] We let the flavor index α run from 1 to N and modify the single occupancy constraint as,

$$\sum_\alpha f_{i,\alpha}^\dagger f_{i,\alpha} = \frac{N}{2}. \tag{7}$$

In addition, we scale the interaction strength $J_{ij}/2$ to be J_{ij}/N to make each term of the Hamiltonian to be of order N. The resulting large-N Hamiltonian is given by

$$H = -\sum_{\alpha,\beta=1}^{N}\sum_{\langle ij\rangle} \frac{J_{ij}}{N} f_{i,\alpha}^\dagger f_{j,\alpha} f_{j,\beta}^\dagger f_{i,\beta}. \tag{8}$$

To treat the quartic interactions we perform a mean-field decoupling by introducing SU(N) singlet valence band, $\chi_{ij} \equiv \frac{1}{N}\Sigma_\alpha \langle f_{i,\alpha}^\dagger f_{j,\alpha}\rangle$. Assuming the valence-band amplitude is a complex number, we obtain the mean-field Hamiltonian given by

$$H_{MF} = -\sum_\alpha \sum_{\langle ij\rangle} J_{ij}(f_{i,\alpha}^\dagger f_{j,\alpha}\chi_{ij}^* + \text{H.c.}) + N\sum_{\langle ij\rangle} J_{ij}|\chi_{ij}|^2 + \sum_{i,\alpha} \mu_i \left(f_{i,\alpha}^\dagger f_{i,\alpha} - \frac{N}{2}\right). \tag{9}$$

Since the fluctuations of χ_{ij} and the average local density $\frac{1}{N}\Sigma_\alpha \langle f_{i,\alpha}^\dagger f_{i,\alpha}\rangle$ scale as $1/\sqrt{N}$, we can safely neglect those fluctuations in the large-N limit justifying the mean-field approximation.

Here we consider the following mean-field Ansatz $\bar{\chi}_{ij} = |\chi_{ij}| e^{i\phi_{ij}}$ where $|\chi_{ij}| = \chi_e$ on expanded links and $|\chi_{ij}| = \chi_t$ on triangular links, respectively. We specify the various flux patterns inside the elementary plaquettes, i.e., the triangles and the dodecagons. The flux inside a triangle $\Phi_\triangle$, for example, is defined in the following way, $e^{i\Phi_\triangle} \equiv e^{i(\phi_{ij}+\phi_{jk}+\phi_{ki})}$, where $\langle ijk\rangle$ indicates the three corners of a triangle traversed along the counterclockwise direction. The flux inside a dodecagon is also defined in the same manner. Since the flux inside a closed loop is a gauge invariant object, different spin liquid Ansatz can be distinguished based on the flux values inside the elementary plaquettes. In particular, we use the term SL[$\Phi_\triangle, \Phi_\nabla, \Phi_{dodecagon}$] to represent the Ansatz which has the fluxes $\Phi_\triangle$ inside an up-pointing triangle, Φ_∇ inside a down-pointing triangle and $\Phi_{dodecagon}$ inside a dodecagon. With a given flux configuration we determine $|\chi_{ij}|$ and μ_i self-consistently by solving the following coupled mean-field equations:

$$\frac{1}{N_{site}}\sum_i \sum_\alpha \langle f_{i,\alpha}^\dagger f_{i,\alpha}\rangle = \frac{N}{2},$$

$$\chi_{ij} = \frac{1}{N}\sum_\alpha \langle f_{i,\alpha}^\dagger f_{j,\alpha}\rangle, \tag{10}$$

where N_{site} is the number of lattice sites.

B. Properties of competing spin liquid phases

In this section we discuss the characteristic properties of various spin liquid phases and their instabilities. In particular, we focus on translationally invariant mean-field states which have nonzero $|\chi_{ij}|$ on every link of the lattice. Extensive discussion on possible dimerized phases is given later in Sec. III. As shown in the previous studies about the spin liquid phases on the square[35] and kagome[7,36] lattices, the inclusion of additional spin interactions can change the relative energetics of different spin liquid phases. Therefore it is useful to understand the nature of various competing spin

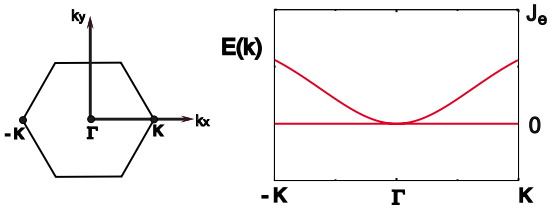

FIG. 2. (Color online) The spinon dispersion of the SL[0,0,0] near the Fermi level. Among the six bands inside the first Brillouin zone we plot the third and four band which are lying close to the Fermi energy along the k_x axis. The flatband is lying at the Fermi level which touches with the dispersive band at the Γ point.

liquid states which are the potential ground states of spin Hamiltonians beyond the nearest-neighbor Heisenberg model.

1. SL [0,0,0]: Uniform spin liquid state

To describe this state we introduce two real mean-field order parameters, χ_e and χ_t, which lie on the expanded and triangular links, respectively. Since the unit cell contains six sites we obtain six different bands inside the first Brillouin zone. Among the six bands, the third and fourth bands near the Fermi level show an interesting structure displayed in Fig. 2. There is a flatband lying on the Fermi energy which is touching another dispersive band at the zone center, $\Gamma(\mathbf{k}=\mathbf{0})$. The flatband comes from the existence of the localized eigenstates, which occur due to the destructive interference of hopping amplitudes between the localized units.[37] The flatband of the uniform spin liquid on the kagome lattice emerges owing to the same reason. However, in contrast to the kagome lattice problem, the flatband is lying exactly at the Fermi level on the star lattice.

The flatness of the band at the Fermi energy is not the generic property of the uniform spin liquid. There are perturbations which do not break any lattice symmetry but spoil the flatness by generating curvature. The third nearest-neighbor hopping is such an example. However, the quadratic degeneracy at the zone center is protected by the point-group symmetry of the underlying unit cell.

To understand the stability of the spin liquid we derive the low-energy effective Hamiltonian, which describes the states near the zone center, expanding the Hamiltonian up to the quadratic order of the momentum $\mathbf{k}$. The procedure for deriving the effective Hamiltonian is outlined in Appendix C. The resulting Hamiltonian is given by

$$H_{\text{eff}} = \frac{1}{m_{\text{eff}}} \int \frac{d^2\mathbf{k}}{(2\pi)^2} \psi^\dagger(\mathbf{k}) h_{\text{eff}}(\mathbf{k}) \psi(\mathbf{k}),$$

in which

$$h_{\text{eff}}(\mathbf{k}) = (k_x^2 + k_y^2)\tau_0 - (k_x^2 - k_y^2)\tau_z - 2k_x k_y \tau_x,$$

where the Pauli matrix τ_i is acting on the two-component space of the continuum field $(\psi)^T = (\psi_1, \psi_2)$ which describes the two low-energy states near the Γ point.

The SL[0,0,0] state respects all the space-group symmetry of the lattice. In particular, if we choose the gauge in which $\chi_{ij} = \chi_t$ on every triangular link and $\chi_{ij} = \chi_e$ on every expanded link with χ_t and χ_e being real constants, the action of the symmetry generators on the spin operator, S_i, is the same as that on the spinon operator, $f_{i,\sigma}$. Since we consider the low-energy excitations near the zone center, we focus on the action of the point-group symmetry on the continuum fields. The D_6 point group of the star lattice consists of 12 symmetry generators and is generated by the two elements, $C_{\pi/3}$ and R_y. Here $C_{\pi/3}$ means the $\frac{\pi}{3}$ rotation with respect to the center of a dodecagon and R_y indicates the reflection about the x axis. The details on the elements of the D_6 point group are discussed in Sec. III B.

Under the $C_{\pi/3}$ and R_y, the continuum field ψ transforms in the following way:

$$C_{\pi/3}: \psi \to e^{-\iota(\pi/3)\tau_y}\psi,$$

$$R_y: \psi \to \tau_z \psi, \tag{11}$$

meaning all the fermion bilinears $\psi^\dagger \tau_\alpha \psi$ $(\alpha = \mathrm{x}, \mathrm{y}, \mathrm{z})$ are forbidden by the point-group symmetry. Note that the $\psi^\dagger \tau_y \psi$ breaks time-reversal symmetry as well since it shows sign change under complex conjugation.

Next we consider the fermion bilinear terms that contain spatial derivatives. Because the dynamical critical exponent is two, the terms with a single spatial derivative are relevant and those with two spatial derivatives are marginal perturbations. Investigating the transformation rule under the D_6 point-group symmetry, it can be easily checked that $\psi^\dagger \tau_y \psi$ transforms as the one-dimensional A_2 irreducible representation and $(\psi^\dagger \tau_x \psi, \psi^\dagger \tau_z \psi)$ forms a basis for the two-dimensional E_2 irreducible representation.[38] Similarly, the transformation properties of derivative terms can be determined. At first, the linear derivative term, (∂_x, ∂_y) transforms as a two-dimensional E_1 irreducible representation. To have terms with linear derivatives in the Hamiltonian, the product of the fermion bilinear and the derivative must be invariant under the point-group symmetry operations. Using the decompositions of $E_1 \otimes A_2 = E_1$ and $E_1 \otimes E_2 = B_1 \oplus B_2 \oplus E_1$, we see that every product of fermion bilinears and the linear derivative is not invariant under the point-group symmetry. Therefore linear derivative terms are not allowed. On the other hand, we have a second derivative term $(\partial_x^2 - \partial_y^2, \partial_x \partial_y)$ making a two-dimensional E_2 irreducible representation. Using $E_2 \otimes A_2 = E_2$ and $E_2 \otimes E_2 = A_1 \oplus A_2 \oplus E_2$, we see that there is a term following A_1 irreducible representation, which is nothing but $\psi^\dagger[(2\partial_x \partial_y)\tau_x + (\partial_x^2 - \partial_y^2)\tau_z]\psi$. Therefore in addition to the isotropic $\psi^\dagger(\partial_x^2 + \partial_y^2)\psi$ term, $\psi^\dagger[(2\partial_x \partial_y)\tau_x + (\partial_x^2 - \partial_y^2)\tau_z]\psi$ is the only term allowed by symmetry. Since these terms are already present in the Hamiltonian, the low-energy properties of the SL[0,0,0] are not spoiled by these marginal perturbations. However, these perturbations add curvature to the flatband.

Finally, we discuss the effect of the four fermion interaction terms on the stability of the SL[0,0,0] state. Though a simple power counting shows that the four fermion interactions are marginal, they are actually marginally relevant. Recently, the effects of the four fermion interaction on the quadratic band crossing are studied using the renormalization group approach.[39,40] According to Ref. 39, the leading weak-

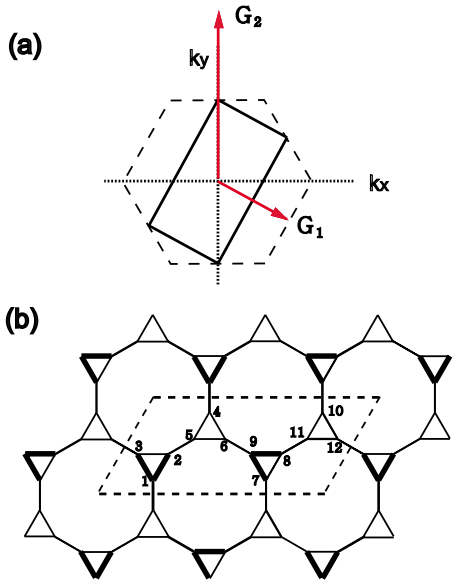

FIG. 3. (Color online) (a) The reduced Brillouin zone (the solid line) corresponding to the doubled unit cell along the $\mathbf{a}_1$ direction. $\mathbf{G}_1$ and $\mathbf{G}_2$ indicate the reciprocal lattice vector corresponding to the doubled unit cell. (b) The flux configuration of the SL$[0,0,\pi]$ state. The 12-site unit cell is surrounded by a dotted box. We assign $-1(+1)$ for the hopping amplitude on the thick (thin) bond.

coupling instability leads to the state with nonzero $\langle \psi^\dagger \tau_y \psi \rangle$, breaking the time-reversal symmetry. It means that SL[0,0,0] state is unstable toward a chiral spin liquid state supporting chiral edge states.

2. SL$[0,0,\pi]$ *state*

The SL$[0,0,\pi]$ state supports π flux piercing the dodecagons. Even though this state does not break the translational symmetry, the mean-field description requires doubling of the unit cell. Here we consider the doubling of the unit cell along the $\mathbf{a}_1$ direction. For the lattice vectors $2\mathbf{a}_1$ and $\mathbf{a}_2$, the reciprocal lattice vectors are given by

$$\mathbf{G}_1 = \left(\frac{\pi}{2}, -\frac{\pi}{2\sqrt{3}}\right), \quad \mathbf{G}_2 = \left(0, \frac{2\pi}{\sqrt{3}}\right).$$

The reduced Brillouin zone corresponding to the above reciprocal lattice vectors is depicted in Fig. 3(a).

For the mean-field description of the SL$[0,0,\pi]$ state, we have chosen the flux configuration as described in Fig. 3(b). Since there are 12 sites inside the unit cell, we have 12 bands within the Brillouin zone. The mean-field spinon dispersion of the low-energy bands near the Fermi level is described in Fig. 4. This state does not have a spinon Fermi surface and shows a gapped spectrum. The lower flatband (valence band) is doubly degenerate and the upper band (conduction band) is dispersive.

According to the projected wave-function study that is discussed in detail later in Sec. IV B, the SL$[0,0,\pi]$ state has the lowest ground-state energy among the various spin liquid Ansatz over a wide parameter range. Unfortunately, however, the SL$[0,0,\pi]$ state is unstable once gauge fluctuation is allowed. Since the spinon spectrum has a finite

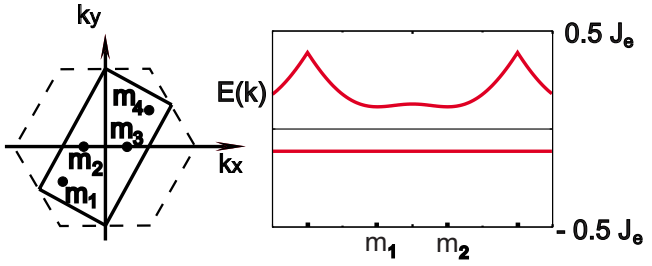

FIG. 4. (Color online) The low-energy spinon bands of the SL$[0,0,\pi]$ state near the Fermi level. The lower band (valence band) is flat and doubly degenerate. The upper band (conduction band) has small dispersion. The locations of the conduction-band minimum are described by $\mathbf{m}_i$. The dispersion is plotted along the $k_y = \sqrt{3}k_x + \frac{\pi}{2\sqrt{3}}$ line passing the $\mathbf{m}_1$ and $\mathbf{m}_2$.

gap, the low-energy excitations are described by the compact U(1) gauge theory. In 2+1 dimension, the compact U(1) gauge theory is confining,[26] which means that free spinons with unit gauge charge can only make charge neutral bound states. In addition, the interaction between spinons can also induce various kinds of broken symmetry states. Extensive discussion on the instability of the SL$[0,0,\pi]$ state and its relation with candidate valence-bond solid phases are given in Sec. V.

3. SL$[\frac{\pi}{2},\frac{\pi}{2},\pi]$: *A chiral spin liquid state*

Next we consider flux phases which possess finite flux inside triangles. A triangle that supports $\frac{\pi}{2}$ flux breaks time-reversal and parity symmetry but preserves the combination of them. A convenient way to investigate the time-reversal symmetry breaking in spin systems is to consider the expectation value of the scalar spin chirality operator[25] defined as follows:

$$\hat{C}_{ijk} \equiv \mathbf{S}_i \cdot (\mathbf{S}_j \times \mathbf{S}_k). \tag{12}$$

Since $\hat{C}_{ijk}$ is odd under both the time-reversal (T) and parity operations, the ground state breaks both symmetries when the expectation value of the scalar spin chirality operator $\langle \hat{C}_{ijk} \rangle$ is nonzero. In other words, the scalar spin chirality plays the role of the order parameter measuring time-reversal symmetry breaking.

Because the unit cell contains two triangles, we can define the following two different scalar spin chirality operators:

$$\hat{C}_{uniform} \equiv \mathbf{S}_1 \cdot (\mathbf{S}_2 \times \mathbf{S}_3) + \mathbf{S}_4 \cdot (\mathbf{S}_5 \times \mathbf{S}_6),$$

$$\hat{C}_{staggered} \equiv \mathbf{S}_1 \cdot (\mathbf{S}_2 \times \mathbf{S}_3) - \mathbf{S}_4 \cdot (\mathbf{S}_5 \times \mathbf{S}_6), \tag{13}$$

where $\hat{C}_{uniform}$ and $\hat{C}_{staggered}$ are the uniform and staggered scalar spin chiralities, respectively. To understand the symmetry properties of the $\hat{C}_{uniform}$ and $\hat{C}_{staggered}$ we have to recognize that there are two different reflection symmetries on the star lattice. The reflection (P_1) with respect to the axis connecting the center of a dodecagon with the midpoint of an expanded link [for example, the a axis in Fig. 12(a)] interchanges the up-pointing triangles and the down-pointing tri-

angles. On the other hand, the other reflection (P_2) about the axis connecting the center of a dodecagon with a vertex of a triangle [for example, the A axis in Fig. 12(a)], leaves each triangle as it is. Under the P_2 reflection both $\hat{C}_{uniform}$ and $\hat{C}_{staggered}$ change their signs. Here we use the term parity to indicate the P_1 reflection symmetry. Note that the parity operation is equivalent to the reflection in two-dimensional space.

$\hat{C}_{uniform}$ is odd under both the time-reversal (T) and parity (P_1) but even under inversion (I). On the other hand $\hat{C}_{staggered}$ is odd under time-reversal and inversion but even under parity. Here the inversion operation is defined with respect to the midpoint of the expanded link connecting two triangles. In both cases, the combination of the time reversal, parity transformation, and inversion (TP_1I) is equivalent to the identity operation under which both the $\hat{C}_{uniform}$ and $\hat{C}_{staggered}$ are invariant.[41]

The SL$[\frac{\pi}{2},\frac{\pi}{2},\pi]$ is characterized by nonzero $\hat{C}_{uniform}$ but with vanishing $\hat{C}_{staggered}$. Therefore it breaks time reversal and parity transformation while it is invariant under the combined operation. It is a chiral spin liquid state which has a finite energy gap. In Fig. 6(a) we plot the spinon dispersion near the Fermi level corresponding to the valence and conduction bands. The energy gap is minimum at the momentum $\mathbf{Q}=(\pi/3,0)$ and $-\mathbf{Q}$. If we expand the mean-field Hamiltonian near the dispersion minimum, $\mathbf{Q}$ and $-\mathbf{Q}$ in the limit of large J_t/J_e, we can get the following effective low-energy Hamiltonian:

$$H_{eff}=\int \frac{d^2q}{(2\pi)^2}\Psi^{\dagger}(q)\{v_F[q_x\tau_x+q_y\tau_y]-m\tau_z\}\Psi(q), \tag{14}$$

where the Fermi velocity $v_F=J_e\chi_e/\sqrt{3}$ and the mass $m=(J_e^2\chi_e^2)/(\sqrt{3}J_t\chi_t)$. In the above we define the eight component Dirac fermion field, $\Psi^{\dagger}=(\varphi^{\dagger}_{1,\alpha,\sigma},\varphi^{\dagger}_{2,\alpha,\sigma})$ in which 1 and 2 are the two-component Dirac indices, α and σ are indices for the nodes ($\pm\mathbf{Q}$) and spins. The Pauli matrix τ_ν acts on the two-component Dirac space. For later convenience we define two additional Pauli matrices, $\vec{\mu}$ and $\vec{\sigma}$ acting on the nodal and spin spaces, respectively.

Since the mass term has the same sign in the two nodal positions, integrating out fermions leads to the Chern-Simons gauge field action. As a consequence, the charge neutral spinon Hall conductivity should be finite. The Chern-Simons term stabilizes the spin liquid ground state by providing a finite mass to the U(1) gauge field. Therefore the U(1) gauge field can only mediate a short-range interaction between the spinons, which makes the fractionalized particles (the spinons) to be the elementary excitations of the spin liquid ground state.[33]

4. SL$[-\frac{\pi}{2},\frac{\pi}{2},0]$: *A nematic spin liquid state*

The SL$[-\frac{\pi}{2},\frac{\pi}{2},0]$ is characterized by nonzero $\hat{C}_{staggered}$ but with vanishing $\hat{C}_{uniform}$. Therefore it breaks both the time-reversal and inversion operations but is invariant under the parity transformation. Because the fluxes of the two triangles within the unit cell have opposite sign, the sixfold rotational symmetry is broken down to the threefold symmetry [see Fig. 5(b)]. Thus it is a nematic spin liquid.

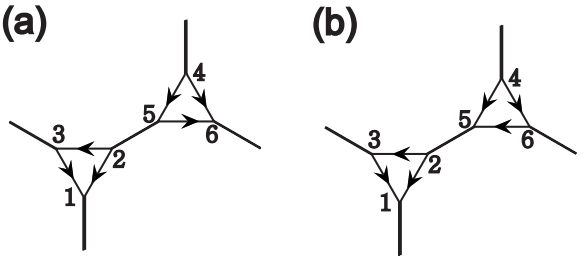

FIG. 5. Flux configuration of the Ansatz SL$[\frac{\pi}{2},\frac{\pi}{2},\pi]$ and SL$[-\frac{\pi}{2},\frac{\pi}{2},0]$. Hopping along (against) the direction of an arrow induce a phase $\pi/2$ ($-\pi/2$). (a) The flux pattern for SL$[\frac{\pi}{2},\frac{\pi}{2},\pi]$. Counterclockwise motion along an triangular link results in the flux $\frac{\pi}{2}$ (b) The flux pattern for SL$[-\frac{\pi}{2},\frac{\pi}{2},0]$. Counterclockwise motion along an up-pointing (down-pointing) triangular link results in the flux $-\frac{\pi}{2}$ ($\frac{\pi}{2}$).

The mean-field spinon dispersion corresponding to the two bands near the Fermi energy is plotted in Fig. 6(b). The spin liquid Ansatz has a spinon Fermi surface which consists of an electron pocket at the $\mathbf{K}=(2\pi/3,0)$ point and a hole pocket at the $-\mathbf{K}$ point.

Expanding the mean-field Hamiltonian using $J_e\chi_e/J_t\chi_t$ as an expansion parameter, the following effective low-energy Hamiltonian can be obtained:

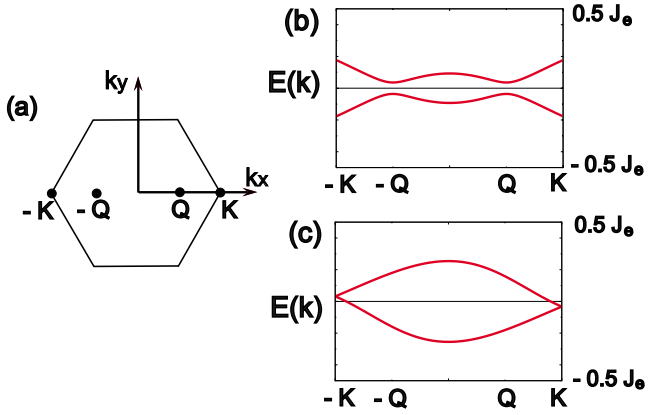

FIG. 6. (Color online) The mean-field spinon band structure of the Ansatz SL$[\frac{\pi}{2},\frac{\pi}{2},\pi]$ and SL$[-\frac{\pi}{2},\frac{\pi}{2},0]$ along the k_x axis when $J_t=2J_e$. (a) The first Brillouin zone. Here Q and $-Q$ denote the points in which minimum (maximum) of the conduction (valence) band of the SL$[\frac{\pi}{2},\frac{\pi}{2},\pi]$ occurs. The K and $-K$ indicate the points where the linear band touching between the two bands near the Fermi energy of the SL$[-\frac{\pi}{2},\frac{\pi}{2},0]$ occurs. (b) The dispersion of the valence and conduction band corresponding to the SL$[\frac{\pi}{2},\frac{\pi}{2},\pi]$ Ansatz. The low-energy excitation near the $\pm Q$ can be described by the massive Dirac particles. (c) The dispersions of the two bands near the Fermi level for SL$[-\frac{\pi}{2},\frac{\pi}{2},0]$. The low-energy excitation near the $\pm K$ point can be described by the Dirac particles under the staggered chemical potential.

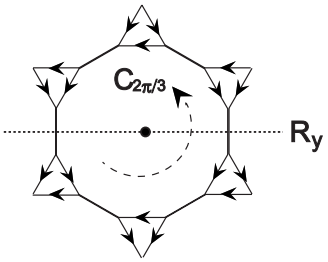

FIG. 7. The generators of the point-group symmetry of the SL$[-\frac{\pi}{2},\frac{\pi}{2},0]$. R_y maps y to $-y$ while $C_{2\pi/3}$ induce the rotation by $2\pi/3$ with respect to the center of the dodecagon.

$$H_{eff}=\int \frac{d^2q}{(2\pi)^2}\Psi^\dagger(q)\{v_F[q_x\tau_x+q_y\tau_y]-M\mu_z\}\Psi(q), \tag{15}$$

where the Fermi velocity $v_F=J_e\chi_e/\sqrt{3}$ and the "staggered" field $M=(J_e^2\chi_e^2)/(\sqrt{3}J_t\chi_t)$. Since the effective chemical potentials coming from the staggered field M have the opposite signs at the two nodal points, we have both an electron pocket (at the **K** point) and a hole pocket (at the **−K** point) on the Fermi surface.

In contrast to the SL$[\frac{\pi}{2},\frac{\pi}{2},\pi]$ state which has a gapped spinon spectrum, the SL$[-\frac{\pi}{2},\frac{\pi}{2},0]$ state has gapless low-energy excitations. To confirm that the low-energy description based the above effective Hamiltonian in Eq. (15) is valid after including the fluctuation beyond the mean-field description, we have to check whether there are relevant perturbations which are allowed by symmetry. Especially, some of the fermion bilinears, which are made of Ψ, can potentially generate various mass terms which spoil the low-energy description of Eq. (15).

To judge the stability of this spin liquid state, we have to understand how the symmetries of the microscopic Hamiltonian are realized in the effective continuum theory. Even though the original spin Hamiltonian is invariant under the full space-group transformations, after the gauge theory formulation of the problem, the symmetry of the mean-field Hamiltonian is realized projectively. That is, under the symmetry transformation S with the mapping $\mathbf{i}\rightarrow S(\mathbf{i})$, the spinon operator $f_{\mathbf{i},\sigma}$ transforms in the following way:

$$S: f_{\mathbf{i},\sigma}\rightarrow G_S(\mathbf{i})f_{S(\mathbf{i}),\sigma},$$

where $G_S(\mathbf{i})$ is a phase factor which depends on the symmetry operation S, and a local coordinate **i**. The group of the symmetry operations which make the mean-field Hamiltonian invariant is called the projective symmetry group (PSG).[42,43]

To perform the PSG analysis we have to specify the symmetry group of the spin Hamiltonian. The star lattice has the D_6 point-group symmetry generated by the sixfold rotation symmetry with respect to the center of a dodecagon and the reflections. However, due to the finite fluxes inside triangles, the SL$[-\frac{\pi}{2},\frac{\pi}{2},0]$ state breaks some D_6 point-group symmetries. Especially, the sixfold rotational symmetry is broken down to threefold rotational symmetry. The point-group symmetry of the SL$[-\frac{\pi}{2},\frac{\pi}{2},0]$ state is generated by the $2\pi/3$ rotation ($C_{2\pi/3}$) around the center of the dodecagon and the reflection (R_y) which maps y to $-y$. The symmetry operations which generate the point group of the SL$[-\frac{\pi}{2},\frac{\pi}{2},0]$ state are depicted in Fig. 7. The SL$[-\frac{\pi}{2},\frac{\pi}{2},0]$ state is also invariant under the translations (T_{a1} and T_{a2}) by the lattice vectors $\mathbf{a}_1$ and $\mathbf{a}_2$. In combination with the above point-group symmetry, the translational symmetry defines the space group of the SL$[-\frac{\pi}{2},\frac{\pi}{2},0]$ state. In addition, the SL$[-\frac{\pi}{2},\frac{\pi}{2},0]$ state is invariant under the combination (TI) of the time reversal (T) and inversion (I) as well as the spin rotation. Finally, it has the charge conjugation symmetry (C^*) via the mapping $f_{i\alpha}\rightarrow\epsilon_i f_{i\alpha}^\dagger$, where $\epsilon_i=1$ for $i=1$, 2 and 3 and -1 for $i=4,5,6$. Under these symmetry operations the continuum field Ψ transforms as follows:

$$\begin{aligned}
T\cdot I&:\Psi\rightarrow(\imath\sigma_y)\tau_x\Psi,\\
C^*&:\Psi\rightarrow(\imath\tau_x)[\Psi^\dagger]^T,\\
T_{a_1}&:\Psi\rightarrow e^{-\imath(2\pi/3)\mu_z}\Psi,\\
T_{a_2}&:\Psi\rightarrow e^{\imath(2\pi/3)\mu_z}\Psi,\\
R_y&:\Psi\rightarrow\mu_z\tau_x\Psi,\\
C_{2\pi/3}&:\Psi\rightarrow e^{-\imath(2\pi/3)\tau_z}\Psi.
\end{aligned} \tag{16}$$

Using the above transformation rules we can easily check that $\Psi^\dagger\mu_z\Psi$ is the only fermion bilinear which is allowed by symmetry. Therefore the low-energy Hamiltonian in Eq. (15) is valid even after we include the fluctuations and protected by the projective symmetry group. Some details about how we have determined the transformation rule of the continuum fields are explained in Appendix B.

Next we discuss about possible instability of the SL$[-\pi/2,\pi/2,0]$ state. The low-energy effective Hamiltonian [Eq. (15)] which is obtained from the perturbative expansion in powers of $J_e\chi_e/J_t\chi_t$ implies that the electron pocket (at the **K** point) and the hole pocket (at the **−K** point) are nested in the large J_t/J_e limit. Therefore the instability in the particle-hole channel with the momentum $2\mathbf{K}$ is expected. The following two fermion bilinears, $\hat{m}_x=\Psi^\dagger\tau_z\mu_x\Psi$ and $\hat{m}_y=\Psi^\dagger\tau_z\mu_y\Psi$, are especially important in this respect. Addition of the mass term $H_M=M_x\hat{m}_x+M_y\hat{m}_y$ to the effective Hamiltonian in Eq. (15) leads to the mass gap of $2\sqrt{M^2+M_x^2+M_y^2}$. Since these mass terms are anticommuting with the effective Hamiltonian in Eq. (15), the pair $(\hat{m}_x,\hat{m}_y)$ opens the largest mass gap than any other pairs of possible mass terms. Interestingly, $(\hat{m}_x,\hat{m}_y)$ transforms nontrivially under the space-group operations. Its symmetry property is consistent with some ordered state with $\sqrt{3}\times\sqrt{3}$-type translational symmetry breaking. Using the terminology defined in Sec. III B, $(\hat{m}_x,\hat{m}_y)$ transforms as the E_3 irreducible representation under the enlarged point group $G_{P,\mathbf{b}}$. The detailed discussion on the group theory for the star lattice is given in Sec. III B.

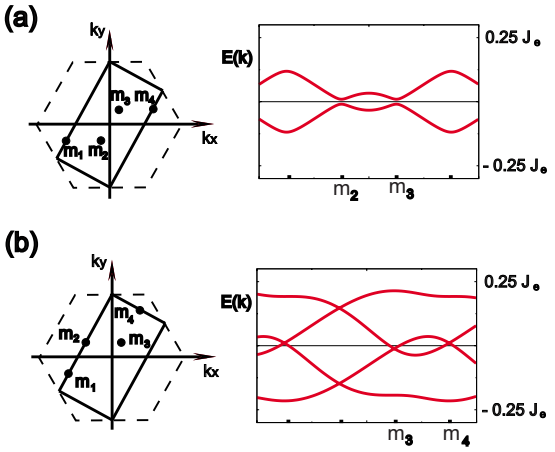

FIG. 8. (Color online) The low-energy spinon bands of the SL$[\frac{\pi}{2},\frac{\pi}{2},0]$ and SL$[-\frac{\pi}{2},\frac{\pi}{2},\pi]$ plotted along the $k_y=\sqrt{3}k_x$ direction. (a) For SL$[\frac{\pi}{2},\frac{\pi}{2},0]$. The locations of the minimum band gap are described by m_i. (b) For SL$[-\frac{\pi}{2},\frac{\pi}{2},\pi]$. Here m_1 and m_3 (m_2 and m_4) indicate the location of the electron (hole) pockets.

5. SL$[\frac{\pi}{2},\frac{\pi}{2},0]$ *and* SL$[-\frac{\pi}{2},\frac{\pi}{2},\pi]$

We obtain SL$[\frac{\pi}{2},\frac{\pi}{2},0]$ (SL$[-\frac{\pi}{2},\frac{\pi}{2},\pi]$) phase by putting additional π flux on every dodecagon on top of SL$[\frac{\pi}{2},\frac{\pi}{2},\pi]$ (SL$[-\frac{\pi}{2},\frac{\pi}{2},0]$) states. Due to the introduction of the additional π flux, the mean-field description requires unit cell doubling although the actual physical wave function maintains the translational invariance.

The spinon dispersion of the SL$[\frac{\pi}{2},\frac{\pi}{2},0]$ state is described in Fig. 8(a). Basically, the structure of the low-energy spectrum of SL$[\frac{\pi}{2},\frac{\pi}{2},0]$ is similar to that of SL$[\frac{\pi}{2},\frac{\pi}{2},\pi]$, except that the number of the momentum points which support low-energy excitations is doubled. Both of them are characterized by finite $\hat{C}_{uniform}$ indicating the time-reversal and parity symmetry breaking. Therefore the SL$[\frac{\pi}{2},\frac{\pi}{2},0]$ state is also a chiral spin liquid state. The low-energy excitations can be described by the effective Hamiltonian similar to Eq. (14) which can be obtained following the same procedure we used to derive Eq. (14) for SL$[\frac{\pi}{2},\frac{\pi}{2},\pi]$.

In Fig. 8(b) we have drawn the low-energy spinon excitation spectrum of the SL$[-\frac{\pi}{2},\frac{\pi}{2},\pi]$ state. There are two electron pockets (around $\mathbf{m}_1$ and $\mathbf{m}_3$) and two hole pockets (around $\mathbf{m}_2$ and $\mathbf{m}_4$). It is characterized by finite $\hat{C}_{staggered}$ showing broken time reversal and inversion symmetry. Since the fluxes inside up triangles and down triangles have opposite signs, the sixfold rotational symmetry is broken down to threefold rotational symmetry. Therefore it is another nematic spin liquid state.

III. DIMER PHASES

A. Large-N approach

According to the pioneering work by Rokhsar,[44] when the lattice system is dimerizable, the best mean-field Ansatz is one of dimerized states in the large-N limit of the SU(N)-generalized Heisenberg model. Here we call a lattice to be dimerizable when it is possible to make every site belong to a dimer and a lattice site be paired with one and only one of its neighboring site. In particular, when every dimer is lying on the link which has the maximum exchange coupling J_{max}, the dimer state belongs to the ground-state manifold of the mean-field Hamiltonian. In terms of the variable χ_{ij}, we have finite $\bar{\chi}_{ij}$ only on the dimers lying on the link which has the maximum spin coupling J_{max}.

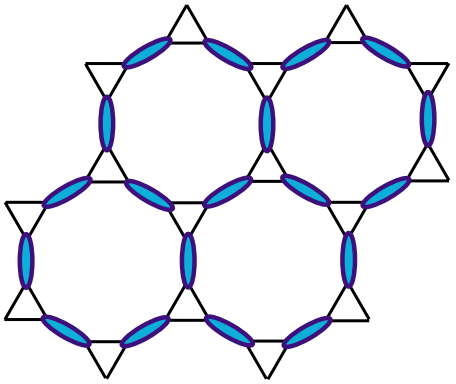

FIG. 9. (Color online) The J_e-dimer VBS state. This is the ground state in the large-N limit when $J_e > J_t$.

The star lattice is dimerizable with respect to J_e. Therefore when J_e is larger than J_t, it has a unique dimerized ground state (we call it the J_e-dimer VBS) in which every dimer is lying on an expanded link connecting neighboring triangles. In Fig. 9 we describe the geometric arrangement of singlet dimers of the J_e-dimer VBS phase.

On the other hand, the Rokhsar's general theorem cannot be applied when J_t is larger than J_e. This is because the star lattice is not dimerizable with respect to the J_t links and every dimer configuration defined on the star lattice contains a finite number of dimers lying on the J_e links. Therefore it is possible that the translationally invariant mean-field Ansatz can be the ground state even in the large-N limit.

When $J_t > J_e$, we have to maximize the number of the dimers lying on triangular links to minimize the ground-state energy of dimerized states. Since every triangle can support a single dimer at most (we call the triangle with a dimer lying on it a filled triangle), the remaining unpaired lattice point of the filled triangle has to be a part of the dimer lying on an expanded link. In other wards, every dimer lying on an expanded link is connecting two filled triangles and this describes a representative local dimer configuration of the

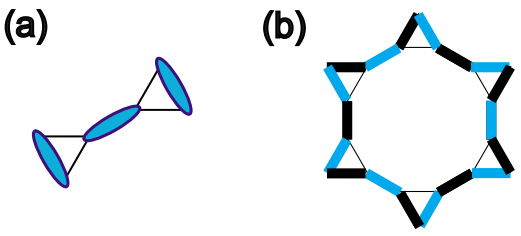

FIG. 10. (Color online) (a) The representative local dimer configuration when $J_t > J_e$. A dimer lying on an expanded link connects two neighboring filled triangles which are supporting dimers on them. (b) The 18-site flippable loop which consists of the alternating bright (blue) and dark (black) thick lines.

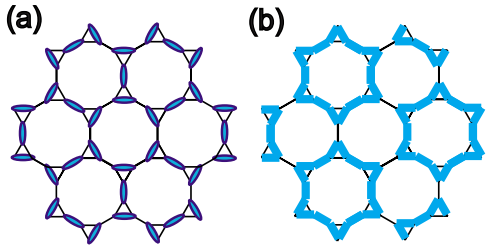

FIG. 11. (Color online) Two low-energy valence-bond solid (VBS) order which are coming from the $1/N$ correction. (a) The columnar 18-site VBS. (b) The box 18-site VBS.

lowest-energy dimerized states when $J_t > J_e$ [see Fig. 10(a)]. Using this local dimer configuration as a building block we can construct infinite number of degenerate dimerized ground states.

To understand how the degeneracy of these dimerized phases is lifted by fluctuations, we consider the $1/N$ corrections to the ground-state energy. In Ref. 22, Read and Sachdev investigated the $1/N$ correction systematically for a similar problem defined on the square lattice. We first review the main ideas of their work briefly and extend the approach to our star lattice problem. For a given dimer configuration, $\bar{\chi}_{ij}$ we include the fluctuations $\delta\chi_{ij}$ as $\chi_{ij}=\bar{\chi}_{ij}+\delta\chi_{ij}$. Here $\bar{\chi}_{ij}$ is nonzero only on the link supporting a dimer lying on it. Expanding the effective action to the quadratic order in the fluctuations, the ground-state degeneracy of the dimerized states on the square lattice could be lifted by the following terms: $\delta S_{eff} \propto N\ \bar{\chi}_{ij}\delta\chi_{jk}\bar{\chi}_{kl}\delta\chi_{li}$. Here i,j,k, and l indicate the four corners of a square plaquette. When a pair of links lying in parallel are occupied by two dimers ($\bar{\chi}_{ij}$ and $\bar{\chi}_{kl}$) and the remaining pair of the links are assigned to the fluctuations ($\delta\chi_{jk}$ and $\delta\chi_{li}$), the δS_{eff} term above can induce additional lowering of the ground-state energy. It means that dimer configurations which support the maximum number of the parallel dimer pairs span the ground-state manifold. The fourfold degenerate columnar valence-bond solid is selected as the ground state following these procedures.

The above idea of the $1/N$ correction can also be rephrased in the following way. For every square plaquette composed of two parallel dimers, we can define a loop which consists of alternating occupied and empty links. Here we call such a loop as a flippable loop[15] because two degenerate dimer configurations are connected via a loop flip, i.e., the interchange of the occupied and empty links. The $1/N$ correction captures the energy lowering through the resonance process which can also be described as a loop flip. The resulting ground state (a columnar dimer state) supports the maximum number of the flippable loops. This idea can be generalized to the higher-order corrections and the degeneracy of dimerized states begins to be lifted from the lowest-order correction corresponding to the smallest flippable loop. Marston and Zeng[23] discussed the effect of the $1/N$ correction on the degeneracy lifting process for the kagome lattice antiferromagnet. There, the first term that lifts the degeneracy involves the six-site flippable loop, which is the so-called perfect hexagon with three dimers on it. The valence-bond solid ground state of the kagome lattice, which contains 36 site within the unit cell, results from the condition of maximizing the number of the perfect hexagons.[15,16,23] The similar idea was also applied to the square-kagome antiferromagnet.[30]

In the star lattice problem with $J_t > J_e$, the dimerized ground states are constructed by repeating the representative local dimer configuration displayed in Fig. 10(a). In this ground-state manifold, the smallest flippable loop contains 18 sites with a dodecagon at the center, which is shown in Fig. 10(b). Here when the bright (blue) thick link is occupied by a dimer, the neighboring dark (black) thick link is empty and vice versa. By interchanging the roles played by the bright (blue) links and the dark (black) links, two degenerate dimerized phases can be connected.

Therefore the fluctuation corrections pick the patterns that maximize the number of the 18-site dimer units participating in the 18-site flippable loops. In Fig. 11(a) we show the valence-bond solid order which has the maximum number of the 18-site flippable loops. Among the six neighboring dodecagons around an 18-site dimer unit, three can be the centers of the 18-site dimer units. This is in contrast to the case of the kagome lattice problem. There, none of the six neighboring hexagons around a perfect hexagon can be perfect hexagons. In fact, the valence-bond solid states on the star lattice have similarity with those on the square lattice. In the case of the square lattice, among the four neighboring square plaquettes around a central plaquette supporting two parallel dimers, half of them (two square plaquettes) can support two parallel dimers. By maximizing the number of the square plaquette composed of two parallel dimers, the columnar valence-bond solid emerges.

Based on the similarity with the square lattice problem, we can call the valence-bond solid in Fig. 11(a) as a columnar 18-site valence-bond solid. In this figure all the dodecagons except the central one support the 18-site dimer unit. The threefold degeneracy of the columnar 18-site VBS comes from the broken translation symmetry. In addition we also consider another low-energy valence-band order which is displayed in Fig. 11(b). Here the 18 links around the 18-site unit have the same finite value of $\bar{\chi}_{ij}$. In analogy with the square lattice problem this phase can be called as the 18-site box VBS phase. The translational symmetry breaking results in the threefold degeneracy in this phase as well. In the recent numerical study by Misguich *et al.*,[29] this phase was suggested as a possible valence-bond solid ground state when $J_t > 1.3J_e$. In contrast to the VBS phases on the square lattice, however, the 18-site columnar VBS phase has lower energy than the 18-site box VBS phase on the star lattice even in the large-N limit. Therefore we propose the 18-site columnar VBS phase as a promising ground-state candidate of the star lattice Heisenberg model for $J_t > J_e$.

B. Group theoretical approach to $\sqrt{3}\times\sqrt{3}$ bond orders

The columnar and box 18-site VBS phases discussed in the above section break the lattice translational symmetry and are described by the enlarged $\sqrt{3}\times\sqrt{3}$ unit cell. Here we perform the detailed symmetry analysis on the bond order that are compatible with the $\sqrt{3}\times\sqrt{3}$ enlarged unit cell.

1. Group theory for the star lattice

The star lattice has the D_6 point-group symmetry. The 12 elements of the D_6 group are as follows:

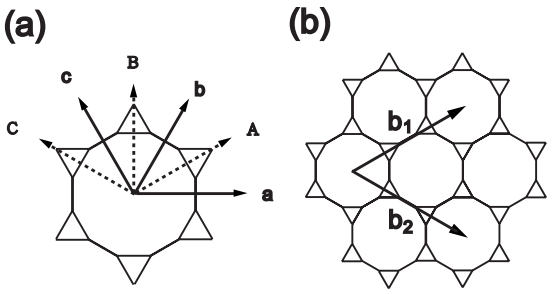

FIG. 12. (a) The intersections between the reflection planes and the lattice plane. (b) The lattice vectors $\mathbf{b}_1$ and $\mathbf{b}_2$ corresponding to the $\sqrt{3}\times\sqrt{3}$ ordered states.

$$D_6 = \{E, C_6, C_6^2, C_6^3, C_6^4, C_6^5, R_a, R_b, R_c, R_A, R_B, R_C\},$$

where C_6 means the rotation by $2\pi/6$ around the center of a dodecagon and E is the identity operator. R_α indicates the reflection with respect to a plane orthogonal to the lattice plane. The reflection planes (denoted by α) are described in the Fig. 12(a).

The space group, G_S, of the star lattice is generated by the translation group, G_T, and the D_6 point group. An element of the space group can be written using the Seitz operator $\{g_{D_6}|\mathbf{t}\}$, where g_{D_6} is an element of the D_6 group and $\mathbf{t}=n_1\mathbf{a}_1+n_2\mathbf{a}_2$. ($n_1$ and n_2 are integers.) The action of a Seitz operator on a lattice point $\mathbf{r}$ is defined as $\{g_{D_6}|\mathbf{t}\}\mathbf{r}=g_{D_6}\mathbf{r}+\mathbf{t}$. Note that the translation group, G_T, is an invariant subgroup of the space group G_S and the point group D_6 is the corresponding factor group, i.e., $D_6=G_S/G_T$.

To understand the symmetry of the enlarged unit cell, we define another translation group, $G_{T,\mathbf{b}}$, whose elements can be written as

$$G_{T,\mathbf{b}} = \{\{E|n_1\mathbf{b}_1 + n_2\mathbf{b}_2\}; n_1, n_2 \in \mathbb{Z}\}, \tag{17}$$

where $\mathbf{b}_1=\mathbf{a}_1+\mathbf{a}_2$ and $\mathbf{b}_2=2\mathbf{a}_1-\mathbf{a}_2$ are the lattice vectors corresponding to the $\sqrt{3}\times\sqrt{3}$ ordered state [see Fig. 12(b)]. Since $G_{T,\mathbf{b}}$ is an invariant subgroup of the space group G_S, the enlarged point group $G_{P,\mathbf{b}}$ can be defined as the factor group $G_{P,\mathbf{b}}=G_S/G_{T,\mathbf{b}}$. Therefore the elements of the space group can be written as $\{g_{G_{P,\mathbf{b}}}|n_1\mathbf{b}_1+n_2\mathbf{b}_2\}$ in which $g_{G_{P,\mathbf{b}}}$ is an element of the enlarged point group, $G_{P,\mathbf{b}}$. (Note that similar approach was used by Hermele *et al.*[10] to investigate the symmetry properties of the object invariant under the translations by $2\mathbf{a}_1$ and $2\mathbf{a}_2$ on the kagome lattice.)

The construction of the $G_{P,\mathbf{b}}$ group is straightforward, whose elements can be written using the Seitz operator $\{g_{D_6}|\bar{\mathbf{t}}\}$ with $\bar{\mathbf{t}}=0$, $\mathbf{a}_1$, $\mathbf{a}_2$. The 36 elements of the $\{g_{D_6}|\bar{\mathbf{t}}\}$ can be grouped into the nine conjugate classes,

$$C_E = \{\{E|0\}\},$$

$$C_T = \{\{E|\mathbf{a}_1\},\{E|\mathbf{a}_2\}\},$$

$$C_6^2 = \{\{C_6^2|0\},\{C_6^4|0\}\},$$

$$C_{6T} = \{\{C_6|0\},\{C_6^5|0\},\{C_6|\mathbf{a}_1\},\{C_6^5|\mathbf{a}_1\},\{C_6|\mathbf{a}_2\},\{C_6^5|\mathbf{a}_2\}\},$$

$$C_{6T}^2 = \{\{C_6^2|\mathbf{a}_1\},\{C_6^4|\mathbf{a}_1\},\{C_6^2|\mathbf{a}_2\},\{C_6^4|\mathbf{a}_2\}\},$$

TABLE I. The character table of the enlarged point group $G_{P,\mathbf{b}}$.

	C_E	C_T	C_6^2	C_{6T}	C_{6T}^2	C_{6T}^3	R_1	R_{1T}	R_{2T}
A_1	1	1	1	1	1	1	1	1	1
A_2	1	1	1	1	1	1	−1	−1	−1
B_1	1	1	1	−1	1	−1	1	1	−1
B_2	1	1	1	−1	1	−1	−1	−1	1
E_1	2	2	−1	1	−1	−2	0	0	0
E_2	2	2	−1	−1	−1	2	0	0	0
E_3	2	−1	2	0	−1	0	2	−1	0
E_4	2	−1	2	0	−1	0	−2	1	0
Q	4	−2	−2	0	1	0	0	0	0

$$C_{6T}^3 = \{\{C_6^3|0\},\{C_6^3|\mathbf{a}_1\},\{C_6^3|\mathbf{a}_2\}\},$$

$$R_1 = \{\{R_a|0\},\{R_b|0\},\{R_c|0\}\},$$

$$R_{1T} = \{\{R_a|\mathbf{a}_1\},\{R_b|\mathbf{a}_1\},\{R_c|\mathbf{a}_1\},\{R_a|\mathbf{a}_2\},\{R_b|\mathbf{a}_2\},\{R_c|\mathbf{a}_2\}\},$$

$$R_{2T} = \{\{R_A|0\},\{R_B|0\},\{R_C|0\},\{R_A|\mathbf{a}_1\},\{R_B|\mathbf{a}_1\},$$
$$\{R_C|\mathbf{a}_1\},\{R_A|\mathbf{a}_2\},\{R_B|\mathbf{a}_2\},\{R_C|\mathbf{a}_2\}\}.$$

Table I displays the character table corresponding to the enlarged point group $G_{P,\mathbf{b}}$. It consists of the four one-dimensional irreducible representations (A_1, A_2, B_1, and B_2) and the four two-dimensional irreducible representations, E_α ($\alpha=1,2,3$, and 4) and a four-dimensional representation Q. Note that the four one-dimensional irreducible representations and the two-dimensional representations E_1 and E_2 are simple extensions of the six irreducible representations of the original D_6 point group. They describe states which are invariant under the lattice translations by $\mathbf{a}_1$ or $\mathbf{a}_2$ as is reflected in the column for C_T in Table I. Therefore the $\sqrt{3}\times\sqrt{3}$-type orderings can be described only through the remaining three irreducible representations E_3, E_4, and Q. It turns out that the two-dimensional irreducible representations E_3 and E_4 are especially important considering the consistency with the numerical result.[29]

2. $\sqrt{3}\times\sqrt{3}$ bond ordering patterns

Here we focus on all possible bond ordering patterns which are compatible with the $\sqrt{3}\times\sqrt{3}$ enlarged unit cell. Labeling the 27 links inside the $\sqrt{3}\times\sqrt{3}$ unit cell by $|l\rangle$, a bond ordering pattern is given by the linear combination of the $|l\rangle$ as

$$|\text{bond order}\rangle \propto \sum_l c_l|l\rangle, \tag{18}$$

where c_l is proportional to the strength of the singlet correlation on the link l, i.e., $c_l \propto -\langle \mathbf{S}_i \cdot \mathbf{S}_j \rangle$. Here i and j denotes the two sites constituting a link l. The vector space spanned by $|l\rangle$ constitutes a reducible representation (defined as Γ_{bond}) of the enlarged point group $G_{P,\mathbf{b}}$ whose decomposition into the irreducible representations is given by

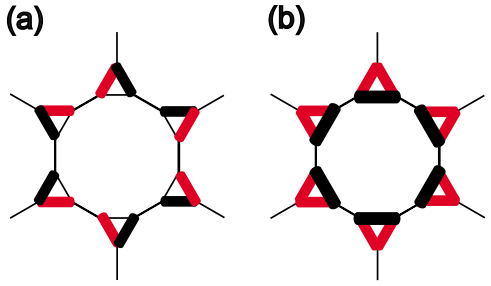

FIG. 13. (Color online) Description of the pair of the E_3^A bond ordered states which form a basis of the E_3 irreducible representation. (a) $c_l=\sqrt{3}$ for the thick light (red) links, $-\sqrt{3}$ for the thick dark (black) links, and zero for the thin solid links. (b) $c_l=1$ for the thick light (red) links, −2 for the thick dark (black) links, and zero for the thin solid links.

$$\Gamma_{\text{bond}} = 2A_1 \oplus B_2 \oplus E_1 \oplus 2E_2 \oplus 2E_3 \oplus E_4 \oplus 3Q.$$

Notice that Γ_{bond} supports two independent E_3 irreducible representations (we call them as E_3^A and E_3^B, respectively) and one E_4 irreducible representation. The bond ordering patterns which constitute a basis of each irreducible representation are displayed in Figs. 13–15 describing E_3^A, E_3^B, and E_4 irreducible representations, respectively.

A bond order transforming as an E_3 irreducible representation can be represented by a linear combination of states like

$$|E_3 \text{ bond order}\rangle = \alpha_1|E_3^A(a)\rangle + \alpha_2|E_3^A(b)\rangle + \alpha_3|E_3^B(a)\rangle + \alpha_4|E_3^B(b)\rangle, \quad (19)$$

in which $|E_3^A(a)\rangle=\Sigma_l c_l|l\rangle$ with c_l specified in Fig. 13(a). The other three basis states $|E_3^A(b)\rangle$, $|E_3^B(a)\rangle$, and $|E_3^B(b)\rangle$ are defined following the same way.

Interestingly the bond ordering patterns of the two valence-bond solid states, the columnar and box 18-site VBS, are given by the following superposition of states:

$$|\text{Columnar VBS}\rangle \propto |\text{uniform}\rangle - |E_3^A(b)\rangle - |E_3^B(b)\rangle,$$

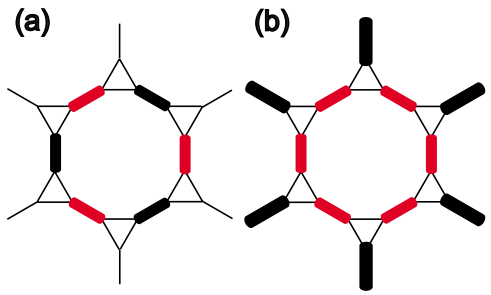

FIG. 14. (Color online) Description of the pair of the E_3^B bond-ordered states which form a basis of the E_3 irreducible representation. (a) $c_l=\sqrt{3}$ for the thick light (red) links, $-\sqrt{3}$ for the thick dark (black) links, and zero for the thin solid links. (b) $c_l=1$ for the thick light (red) links, −2 for the thick dark (black) links, and zero for the thin solid links.

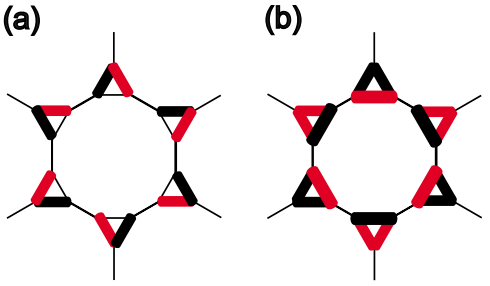

FIG. 15. (Color online) Description of the pair of the E_4 bond-ordered states which form a basis of the E_4 irreducible representation. (a) $c_l=\sqrt{3}$ for the thick light (red) links, $-\sqrt{3}$ for the thick dark (black) links, and zero for the thin solid links. (b) In each triangle the link belonging to the central dodecagon has the $c_l=2$ (−2) if it has red (black) color. The other two links of the triangle have $c_l=1$ (−1) if they have red (black) colors.

$$|\text{Box VBS}\rangle \propto |\text{uniform}\rangle + \frac{1}{2}|E_3^A(b)\rangle + \frac{1}{2}|E_3^B(b)\rangle, \quad (20)$$

where $|\text{uniform}\rangle \equiv \Sigma_l|l\rangle$. Since both the columnar and box 18-site VBS are invariant under the reflections R_a, R_b, and R_c, $|E_3^A(a)\rangle$ and $|E_3^B(a)\rangle$ have no contribution. Superpositions of the $|E_3^A(b)\rangle$ and $|E_3^B(b)\rangle$ can induce more general bond ordering patterns other than those described in Fig. 11. Finally, since E_4 irreducible representation always breaks the reflections R_a, R_b, and R_c (see Fig. 15), we neglect bond orders transforming as E_4 irreducible representation.

IV. GROUND-STATE ENERGY

In this section we compare the ground-state energies of various spin liquid states.

A. Mean-field theory

The ground-state energies of various spin liquid states for $J_t=2J_e$ are shown in Table II. In addition to the translationally invariant spin liquid states with finite J_e and J_t, we have also considered a decoupled dimer phase for comparison. A decoupled dimer phase, which has the lowest mean-field ground-state energy for $J_t>J_e$, can be built based on the local dimer configuration described in Fig. 10(a). The columnar 18-site valence-bond solid (VBS) displayed in Fig. 11(a)

TABLE II. The ground-state energies of the various mean-field Ansatz when $J_t=2J_e$. The energies are measured in unit of J_e.

	E_{MF} (unprojected)	E_{MF} (projected)
Dimer	−0.625	−0.625
SL[0,0,0]	−0.498	−0.647
SL$[\frac{\pi}{2},\frac{\pi}{2},\pi]$	−0.553	−0.624
SL$[-\frac{\pi}{2},\frac{\pi}{2},0]$	−0.553	−0.616
SL$[0,0,\pi]$	−0.498	−0.654
SL$[\frac{\pi}{2},\frac{\pi}{2},0]$	−0.552	−0.617
SL$[-\frac{\pi}{2},\frac{\pi}{2},\pi]$	−0.552	−0.614

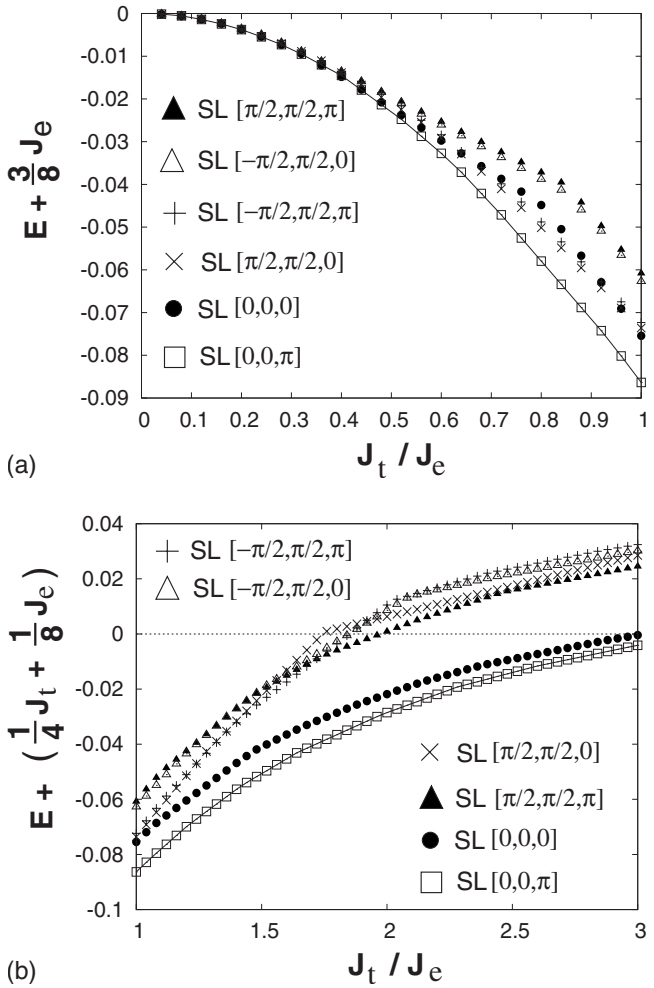

FIG. 16. The ground-state energy per spin of the various spin liquid Ansätze computed using Gutzwiller projection. (a) Energies for $0 \leq J_t/J_e \leq 1$ measured relative to the J_e-dimer VBS state shown in Fig. 9, which has an energy $-3J_e/8$ per spin. (b) Energies for $1 \leq J_t/J_e \leq 3$ measured relative to the $\sqrt{3}\times\sqrt{3}$ VBS state shown in Fig. 11 which has an energy $-J_t/4-J_e/8$ per spin. Note that SL$[0,0,\pi]$ (solid line is a guide to the eyes) has the lowest energy over the whole parameter space. SL[0,0,0] has the second lowest energy for a wide range for $J_t > J_e$. For $J_t=2J_e=2$, the energy per spin of all six spin liquid Ansätze are given in Table II. (These computations were carried out on a system with 6×6 unit cells, i.e., with 216 spins, and the statistical error bars on the energy are of the order of the symbol size.)

is an example. According to the mean-field calculation, the dimer state has lower ground-state energy than any other translationally invariant spin liquids. Among the spin liquid phases with translational invariance, the four Ansatz having the $\pi/2$ flux inside triangles have lower energies than those having zero flux inside triangles, i.e., SL [0,0,0] and SL$[0,0,\pi]$.

B. Projected wave-function study

In the above mean-field calculation, the single occupancy constraint is imposed only on average. Therefore the mean-field wave functions contain unphysical states with zero or two fermions at a point. To obtain physical spin wave functions we therefore perform a numerical Gutzwiller projection on the mean-field wave functions. The ground-state energies of the projected states are computed numerically using the variational Monte Carlo (VMC) method.[45,46] The resulting energies are displayed in Fig. 16 for a range of J_t/J_e where we have optimized the state with respect to χ_t/χ_e for each value of J_t/J_e. Table II shows the numerical energy values for $J_t/J_e=2.0$ to facilitate a comparison with the mean-field numerics. We find that Gutzwiller projection dramatically changes the relative ordering of the various states and that the state SL$[0,0,\pi]$ appears, upon projection, to be the lowest-energy spin liquid over the entire parameter range. For $J_t/J_e=1$, the variational energy of the SL$[0,0,\pi]$ state is $-0.462J_e$ per spin, which is in good agreement with an exact diagonalization study[28] where the ground-state energy is estimated to be $-0.465J_e$ per spin.

C. Bond operator approach

According to the projected wave-function study, SL$[0,0,\pi]$ state is the ground state over a wide parameter space. However, the SL$[0,0,\pi]$ state is unstable due to the confinement in the 2+1-dimensional pure gauge theory. It is also inconsistent with our expectation for the $J_e \gg J_t$ limit. When $J_e \gg J_t$, the J_e-dimer VBS phase (see Fig. 9) is the exact ground state. In addition the recent exact diagonalization study shows that the J_e-dimer VBS phase remains as the ground state up to the isotropic limit of $J_e=J_t$.[28] Therefore SL$[0,0,\pi]$ state should have higher energy than J_e-dimer VBS phase at least in some finite range of $0 \leq J_t/J_e \leq 1$. This discrepancy comes from the lack of the interdimer interaction in the decoupled dimer limit. For the description of dimerized phases beyond the decoupled dimer limit, we undertake the self-consistent bond operator approach.[47–49] If the correction coming from the interdimer interaction is significant, we also have to check the possibility that the true ground state is a valence-bond solid even when $J_t > J_e$.

In the bond operator formulation, the dimer singlet degrees of freedom are used as natural building blocks and the quantum corrections coming from the triplet fluctuations can systematically be investigated.[50,51] Here we present a brief explanation of the bond operator formulation. Let us consider the two $S=\frac{1}{2}$ spins constituting a dimer singlet, $\mathbf{S}_R$ and $\mathbf{S}_L$. The Hilbert space is spanned by four states that can be taken as a singlet state, $|s\rangle$, and three triplet states, $|t_x\rangle$, $|t_y\rangle$, and $|t_z\rangle$. Then, the singlet and triplet boson operators are introduced such that each of the above states can be created from the vacuum $|0\rangle$ as follows:

$$|s\rangle = s^\dagger|0\rangle = \frac{1}{\sqrt{2}}(|\uparrow\downarrow\rangle - |\downarrow\uparrow\rangle),$$

$$|t_x\rangle = t_x^\dagger|0\rangle = -\frac{1}{\sqrt{2}}(|\uparrow\uparrow\rangle - |\downarrow\downarrow\rangle),$$

$$|t_y\rangle = t_y^\dagger|0\rangle = \frac{i}{\sqrt{2}}(|\uparrow\uparrow\rangle + |\downarrow\downarrow\rangle),$$

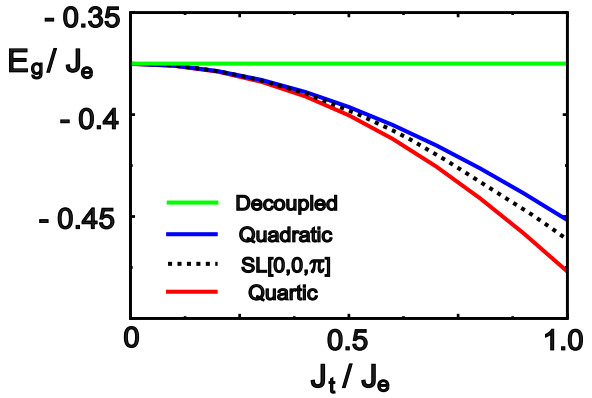

FIG. 17. (Color online) Comparison of the ground-state energy of SL$[0,0,\pi]$ to that of J_e-dimer VBS for $0 \leq J_t/J_e \leq 1$. To emphasize the importance of the interdimer interactions we present the energies of J_e-dimer VBS obtained in three different ways. The "decoupled" indicates the energy of the decoupled dimers. "Quartic" ("quadratic") is the energy from the bond operator theory with (without) the quartic interaction effect.

$$|t_z\rangle = t_z^\dagger|0\rangle = \frac{1}{\sqrt{2}}(|\uparrow\downarrow\rangle + |\downarrow\uparrow\rangle).$$

To eliminate unphysical states from the enlarged Hilbert space, the following constraint needs to be imposed on the bond-particle Hilbert space:

$$s^\dagger s + t_\alpha^\dagger t_\alpha = 1,$$

where $\alpha = x, y$, and z, and we adopt the summation convention for the repeated indices hereafter unless mentioned otherwise.

Constrained by this equation, the exact expressions for the spin operators can be written in terms of the bond operators:

$$S_{R\alpha} = \frac{1}{2}(s^\dagger t_\alpha + t_\alpha^\dagger s - i\varepsilon_{\alpha\beta\gamma} t_\beta^\dagger t_\gamma),$$

$$S_{L\alpha} = \frac{1}{2}(-s^\dagger t_\alpha - t_\alpha^\dagger s - i\varepsilon_{\alpha\beta\gamma} t_\beta^\dagger t_\gamma),$$

where $\varepsilon_{\alpha\beta\gamma}$ is the third-rank totally antisymmetric tensor with $\varepsilon_{xyz} = 1$.

Utilizing the bond operator representation of spin operators, the Heisenberg spin Hamiltonian in Eq. (1) can be rewritten solely in terms of bond particle operators. Since all dimers of J_e-dimer VBS phase are symmetry equivalent, the singlet condensate density $\langle s_\mathbf{i}\rangle$ and the chemical potential $\mu_\mathbf{i}$ can be set to be $\langle s_\mathbf{i}\rangle = \bar{s}$ and $\mu_\mathbf{i} = \mu$ in our mean-field theory. Here $\mathbf{i}$ denotes the location of dimers. The hard-core constraint on the bond-particle operators is imposed by adding the following Lagrange multiplier term, $H_\mu = -\Sigma_\mathbf{i}\mu(\bar{s}^2 + t_{\mathbf{i}\alpha}^\dagger t_{\mathbf{i}\alpha} - 1)$. The resulting Hamiltonian can be written as follows:

$$H = N\epsilon_0 + H_{\text{Quad}} + H_{\text{Quartic}}, \tag{21}$$

where

$$H_{\text{Quad}} = \left(\frac{J_e}{4} - \mu\right)\sum_\mathbf{i} t_{\mathbf{i}\alpha}^\dagger t_{\mathbf{i}\alpha} + \frac{J_t\bar{s}^2}{4}\sum_{\langle\mathbf{i},\mathbf{j}\rangle}\{t_{\mathbf{i}\alpha}^\dagger t_{\mathbf{j}\alpha} + t_{\mathbf{i}\alpha}t_{\mathbf{j}\alpha} + \text{H.c.}\} \tag{22}$$

and

$$H_{\text{Quartic}} = -\frac{J_t}{4}\sum_{\langle\mathbf{i},\mathbf{j}\rangle}\varepsilon_{\alpha\beta\gamma}\varepsilon_{\alpha\mu\nu} t_{\mathbf{i}\beta}^\dagger t_{\mathbf{i}\gamma} t_{\mathbf{j}\mu}^\dagger t_{\mathbf{j}\nu}. \tag{23}$$

In the above, N is the number of unit cells and

$$\epsilon_0 = 3\left[\mu(1-\bar{s}^2) - \frac{3}{4}J_e\bar{s}^2\right]. \tag{24}$$

The quartic interactions between triplet particles are decoupled using the mean- field order parameters P and Q, where $P \equiv \langle t_{\mathbf{i}\alpha}^\dagger t_{\mathbf{j}\alpha}\rangle$ and $Q \equiv \langle t_{\mathbf{i}\alpha} t_{\mathbf{j}\alpha}\rangle$. Here P and Q denote the diagonal and off-diagonal triplet correlations between neighboring dimers. These two order parameters P and Q together with $\bar{s}$ and μ are determined self-consistently by solving the coupled saddle-point equations.[48,49]

The ground-state energy of J_e-dimer VBS phase obtained from the self-consistent bond operator calculation is displayed and compared to the energy of SL$[0,0,\pi]$ state in Fig. 17. Here we have obtained the energy of J_e-dimer VBS phase in three different ways. If we neglect the interdimer couplings (the decoupled dimer limit) completely, the energy is independent of J_t/J_e. The inclusion of the interdimer interaction lowers the ground-state energy significantly. In the end, J_e-dimer VBS phase has the lower ground energy than the SL$[0,0,\pi]$ state over the entire parameter range of $0 \leq J_t/J_e \leq 1$ when we include the quartic interactions. The interdimer interactions generate huge correction to the ground-state energy of dimerized phases.

Now we concentrate on the other limit where $J_t > J_e$. In contrast to the $J_e \gg J_t$ limit, it is nontrivial to identify the ground state even when we restrict our attention to valence-bond solid phases. Taking into account the information from the exact diagonalization study and $1/N$ fluctuation from the large-N limit, we suggest the columnar 18-site VBS phase as a promising candidate for the ground state as explained below.

We apply the bond operator approach to the columnar 18-site VBS phase. The nine dimers within the unit cell can be divided into two groups. One group is made of the six dimers lying on the triangular links. Note that all these six dimers are lying on a dodecagon. [See the central dodecagon in Fig. 11(a).] We call such a dodecagon surrounded by six dimers as a "perfect" dodecagon. The remaining three dimers lying on the expanded links make the other group. Every dimer belonging to the same group is symmetry equivalent as one can easily notice from the patterns around the central "perfect" dodecagon in Fig. 11(a). To apply the bond operator approach we have to introduce two independent sets of order parameters to distinguish the two different groups of dimers. We use $\bar{s}_e$ and μ_e ($\bar{s}_t$ and μ_t) to indicate the singlet condensate density and the chemical potential corresponding to the expanded (triangular) link. To decouple the quartic triplet interactions we introduce two sets of the order parameters, that is, $\{P_{pp}, Q_{pp}\}$ and $\{P_{ep}, Q_{ep}\}$. $P_{pp}(Q_{pp})$ describes

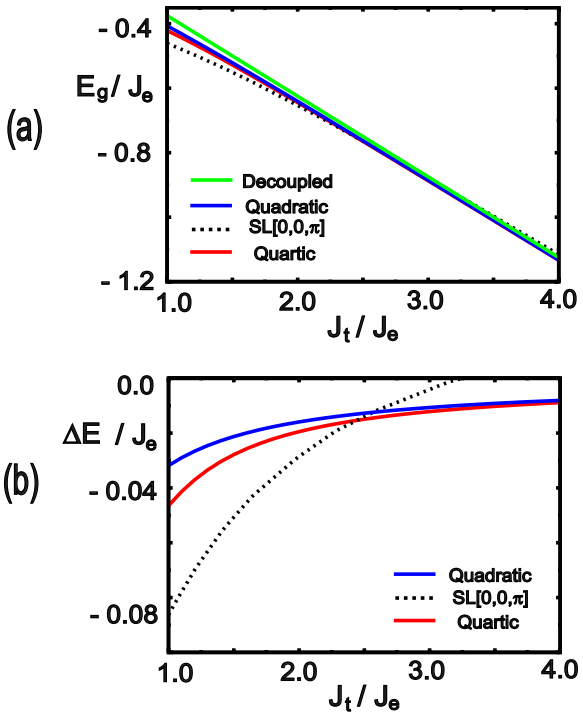

FIG. 18. (Color online) Comparison of the ground-state energies of the columnar 18-site VBS to that of SL$[0,0,\pi]$ state. (a) Energetics for $J_t > J_e$. The energies of the columnar 18-site VBS are obtained in three different ways as in Fig. 17. (b) The relative energies obtained by subtracting the decoupled dimer energy. Note that there is a level crossing around $J_t/J_e \approx 2.4$ between the energy of SL$[0,0,\pi]$ state and that of the columnar 18-site VBS including the quartic interaction.

the diagonal (off-diagonal) correlation between the neighboring dimers lying on a perfect dodecagon. On the other hand $P_{ep}(Q_{ep})$ describes the diagonal (off-diagonal) correlation between a dimer lying on an expanded link and its neighboring dimer lying on a perfect dodecagon. We have determined the eight parameters $\bar{s}_\alpha$, μ_α (α=t or e), and P_β, Q_β (β=pp or ep) self-consistently by solving the coupled saddle-point equations.

The self-consistent solution shows that $P_{ep}=Q_{ep}=0$, $\bar{s}_e^2=1$, and $\mu_e=-3/4J_e$. Since P_{ep} and Q_{ep} describe the coupling between the dimers lying on expanded links and the dimers lying on perfect dodecagons, these two groups of dimers are completely decoupled when $P_{ep}=Q_{ep}=0$. In this situation, every dimer lying on expanded links is decoupled from the surrounding, leading to $\bar{s}_e^2=1$ and $\mu_e=-3/4J_e$. The triplet fluctuations are confined inside every isolated perfect dodecagon, which is reflected in the finite P_{pp} and Q_{pp} values. This interesting structure would result in the highly localized triplet excitation spectrum.

The ground-state energies of the columnar 18-site VBS and SL$[0,0,\pi]$ are compared in Fig. 18. The energies of the columnar 18-site VBS are obtained in three different ways again, that is, for the decoupled dimer limit, including the interdimer coupling neglecting quartic interactions, and finally including the interdimer quartic interactions. For clarity we also calculated the energy difference relative to the decoupled dimer energy as shown in Fig. 18(b). Interestingly,

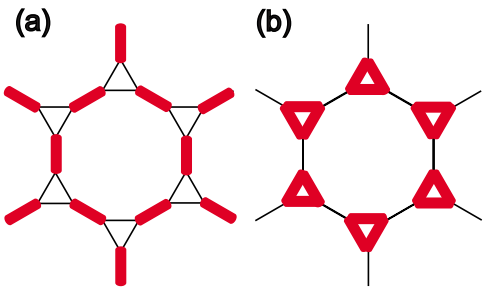

FIG. 19. (Color online) Two bond ordering patterns transforming as the A_1 irreducible representation. The thick solid (red) link has $c_l=1$ while the thin solid link has $c_l=0$. (a) J_e-bond order. (b) J_t-bond order.

there is a critical ratio $(J_t/J_e)_c \approx 2.4$ beyond which the columnar 18-site VBS becomes the ground state when we include the quartic triplet interactions. Even though the critical ratio $(J_t/J_e)_c$ is a bit larger than the suggested phase boundary from the numerical study,[29] the existence of the critical values of $(J_t/J_e)_c$ is quite encouraging. In particular, because the slopes of the lines in Fig. 18(a) are almost parallel, small additional energy correction could induce a large shift of the crossing point as shown in Fig. 18(b). Since the simple Hartree-Fock approximation does not take into account the fluctuations coming from the cooperative interaction between the dimers on the expanded links and those on the perfect dodecagons, we expect that the quantum correction beyond the Hartree-Fock limit could shift the energy-level crossing point down to $(J_t/J_e)_c \approx 1.3$ as suggested by the numerical study.[29]

V. INSTABILITY OF SL$[0,0,\pi]$ SPIN LIQUID AND VALENCE-BOND SOLIDS

Summarizing the previous discussions, J_e-dimer VBS phase is the ground state for $J_t/J_e < (J_t/J_e)_{c1}$ while the columnar 18-site VBS is the ground state in the opposite limit of $J_t/J_e > (J_t/J_e)_{c2}$. [Here $(J_t/J_e)_{c1} \leq (J_t/J_e)_{c2}$.] Although this result is obtained based on the energy comparison with SL$[0,0,\pi]$ state, one may still expect that the two valence-bond solid states are intimately related to the SL$[0,0,\pi]$ state. In particular, the J_e-dimer VBS and the columnar 18-site VBS may arise as a consequence of the confinement in the SL$[0,0,\pi]$ spin liquid state. In this section we describe the possible relation between these two valence-bond solid phases and the SL$[0,0,\pi]$ state.

A. Spinon confinement and uniform bond orders

Due to the finite spinon gap, the U(1) gauge field is the only low-energy excitation in the SL$[0,0,\pi]$ state in the long-wavelength limit. Since the compact U(1) gauge theory without matter field is confining in 2+1 dimension, we expect that the monopole proliferation would lead the SL$[0,0,\pi]$ Ansatz to some confined phases. To understand the properties of the confined phases resulting from the monopole condensation, we have to determine the symmetry properties of the monopole operators.

Here we discuss the possibility that the monopole operators are invariant under all possible symmetry transformations. The J_e-dimer VBS phase, which is the ground state for $J_t/J_e<1$, is invariant under space-group operations. The bond ordering pattern of the J_e-dimer VBS phase belongs to the trivial A_1 irreducible representation of the D_6 point group. Therefore if we interpret the J_e-dimer VBS phase to be induced by the confinement transition, which is reasonable in the limit of $J_t/J_e \ll 1$, this reflects the fact that monopole operators are invariant under symmetry transformations.

Extending the group theory analysis we performed in Sec. III B, we investigate all possible bond orders invariant under the space-group operations. These are displayed in Fig. 19. Here we have finite singlet correlation ($c_l \neq 0$) only on the thick solid (red) links. The bond order in Fig. 19(a) is nothing but the J_e-dimer VBS phase. On the other hand, the bond order in Fig. 19(b) has finite c_l only on the triangular links (we call it as a J_t-bond ordered phase). We expect the J_t-bond ordered phase is the natural low-energy bond ordering pattern when $J_t \gg J_e$. Since the arbitrary superposition of these two orders follows the same A_1 irreducible representation, we expect the actual ground states would have finite c_l values over all the links on the lattice. However, it is natural to expect that the c_l on the expanded (triangular) link would be larger than that on the triangular (expanded) link when $J_e > J_t$ ($J_e < J_t$). Therefore the bond-ordered phase corresponding to the A_1 irreducible representation successfully describes the low-energy manifold over the whole parameter range of J_t/J_e. Interestingly, the recent work by Choy and Kim[52] suggested that the same bond ordered states are the ground states of the same model Hamiltonian in the strong quantum limit based on the bosonic Sp(N) approach.

Since the spinon band structure of the SL$[0,0,\pi]$ state does not change qualitatively by varying J_t/J_e, we expect that the change in J_t/J_e ratio would not affect the trivial monopole quantum number. Therefore if the ordered phase is coming from the confinement transition, it will transform trivially under the symmetry operations. However, it is also possible that the instability of the SL$[0,0,\pi]$ state is caused by the interactions between spinons leading to some broken symmetry phases. We discuss about this possibility in the following section.

B. Instability induced by interactions between spinons

Here we investigate the instability of the SL$[0,0,\pi]$ state coming from the interactions between spinons and the symmetry properties of the resulting ordered phase. Especially we focus on the instability toward the states with the $\sqrt{3}\times\sqrt{3}$-type translational symmetry breaking. As shown in Fig. 4, the valence band is completely flat without any preferred momentum. However, the conduction band supports several dispersion minima. The four minimum points of the conduction band are given by

$$\mathbf{m}_3 = -\mathbf{m}_2 = \left(\frac{\pi}{6},0\right) \quad \text{and} \quad \mathbf{m}_4 = -\mathbf{m}_1 = \left(\frac{\pi}{3},\frac{\pi}{2\sqrt{3}}\right).$$

Interestingly if we double the vectors connecting neighboring minimum points, they sit on the Brillouin zone corners which are nothing but the momentum corresponding to the $\sqrt{3}\times\sqrt{3}$ ordering. Motivated by this observation we study the symmetry properties of the bound states made of low-energy fermions near the conduction-band minima.

We introduce the fermion fields Ψ_i which describe the low-energy excitations near the four conduction-band minima $\mathbf{m}_i$ ($i=1,2,3$, and 4),

$$\Psi_i(\mathbf{x}) \sim \sum_{n=1}^{12} e^{-i\mathbf{m}_i\cdot\mathbf{x}}(\nu_i)_n^* f_n(\mathbf{x}),$$

where ν_i is the eigenvector of the mean-field Hamiltonian at the momentum $\mathbf{m}_i$ and f_n is a slowly varying fermion field near the conduction-band minimum, with n labeling the 12 sites within the unit cell. To determine the symmetry of bound states made of the above low-energy fermions, we have to understand how the symmetries of the microscopic Hamiltonian are realized in the effective continuum fields, Ψ_i. Here we follow the same procedure which we use to determine the transformation properties of the continuum field for the SL$[-\frac{\pi}{2},\frac{\pi}{2},0]$ state in Sec. II B. To extract the necessary information on the transformations of the continuum field, we consider a finite system of a 6×12 unit cell. By solving the mean-field Hamiltonian on this finite system, we determine the properties of the eigenvectors at the four momentum points, $\mathbf{m}_i$. The detailed explanation of the procedure as to how to determine the symmetry of the continuum fields is discussed in Appendix B.

Through the projective symmetry-group analysis, we determine the following transformation properties of the continuum fields:

$$T_{a_1}:\begin{pmatrix}\Psi_1\\ \Psi_3\\ \Psi_2\\ \Psi_4\end{pmatrix}\rightarrow\begin{pmatrix}0 & e^{-i(\pi/3)} & 0 & 0\\ 1 & 0 & 0 & 0\\ 0 & 0 & 0 & 1\\ 0 & 0 & e^{i(\pi/3)} & 0\end{pmatrix}\begin{pmatrix}\Psi_1\\ \Psi_3\\ \Psi_2\\ \Psi_4\end{pmatrix},$$

$$T_{a_2}:\begin{pmatrix}\Psi_1\\ \Psi_3\\ \Psi_2\\ \Psi_4\end{pmatrix}\rightarrow\begin{pmatrix}e^{-i(5\pi/6)} & 0 & 0 & 0\\ 0 & e^{i(\pi/6)} & 0 & 0\\ 0 & 0 & e^{i(\pi/6)} & 0\\ 0 & 0 & 0 & e^{i(5\pi/6)}\end{pmatrix}\begin{pmatrix}\Psi_1\\ \Psi_3\\ \Psi_2\\ \Psi_4\end{pmatrix},$$

$$R_y:\begin{pmatrix}\Psi_1\\ \Psi_3\\ \Psi_2\\ \Psi_4\end{pmatrix}\rightarrow\begin{pmatrix}\frac{-1}{\sqrt{2}} & \frac{-e^{i(\pi/3)}}{\sqrt{2}} & 0 & 0\\ \frac{-e^{-i(\pi/3)}}{\sqrt{2}} & \frac{1}{\sqrt{2}} & 0 & 0\\ 0 & 0 & \frac{1}{\sqrt{2}} & \frac{-e^{i(\pi/3)}}{\sqrt{2}}\\ 0 & 0 & \frac{-e^{-i(\pi/3)}}{\sqrt{2}} & \frac{-1}{\sqrt{2}}\end{pmatrix}\times\begin{pmatrix}\Psi_1\\ \Psi_3\\ \Psi_2\\ \Psi_4\end{pmatrix},$$

$$C_{\pi/3}:\begin{pmatrix}\Psi_1\\ \Psi_3\\ \Psi_2\\ \Psi_4\end{pmatrix}\rightarrow\begin{pmatrix} 0 & 0 & \frac{-1}{\sqrt{2}} & \frac{-e^{i(\pi/3)}}{\sqrt{2}}\\ 0 & 0 & \frac{-ie^{-i(\pi/3)}}{\sqrt{2}} & \frac{i}{\sqrt{2}}\\ \frac{-i}{\sqrt{2}} & \frac{ie^{i(\pi/3)}}{\sqrt{2}} & 0 & 0\\ \frac{-e^{-(i\pi/3)}}{\sqrt{2}} & \frac{-1}{\sqrt{2}} & 0 & 0\end{pmatrix}\times\begin{pmatrix}\Psi_1\\ \Psi_3\\ \Psi_2\\ \Psi_4\end{pmatrix}.$$

We first investigate the symmetry of all possible fermion bilinears which can be written as $\Psi_i^\dagger \mathrm{M}_{ij}\Psi_j$. For the description of the 4×4 unitary matrix M_{ij} we introduce two sets of the Pauli matrices τ_i and μ_j. Here τ_i is acting on the space spanned by either (Ψ_1,Ψ_3) or (Ψ_2,Ψ_4). On the other hand μ_i is defined in the space spanned by (Ψ_1,Ψ_2) or (Ψ_3,Ψ_4). Among the 16 possible bilinears, there are only two terms which can form a basis of the enlarged point group $G_{P,\mathbf{b}}$. These are $\Psi_i^\dagger\tau_3\mu_0\Psi_j$ and $\Psi_i^\dagger\tau_0\mu_0\Psi_j$ which transform as the A_2 and A_1 irreducible representation of the enlarged point group $G_{P,\mathbf{b}}$, respectively. However, since these two bilinears have zero total momentum, they cannot describe the $\sqrt{3}\times\sqrt{3}$-type symmetry breaking. The net momentums carried by the other 14 bilinears are neither zero nor $\mathbf{K}=(\frac{2\pi}{3},0)$. Therefore the transformation properties of them are not compatible with the symmetry of the $\sqrt{3}\times\sqrt{3}$-type enlarged unit cell.

Next we consider the instability in the particle-particle channels. Defining the pairing amplitude as $\Delta_{ij}\equiv\Psi_i\Psi_j$, we have 16 different Δ_{ij}. We first omit the indices for the spin degrees of freedom and study how they transform under the space-group symmetry operations. It can easily be checked that the 16 pairing amplitudes are divided into the four different sets Π_1, Π_2, Ω_1, and Ω_2 which transform independently. The six-component vectors Π_i and the two-component vectors Ω_i are given by

$$\Pi_1=\begin{pmatrix} e^{-i(\pi/3)}\Delta_{11}+e^{i(\pi/3)}\Delta_{33}\\ e^{-i(\pi/3)}\Delta_{11}-e^{i(\pi/3)}\Delta_{33}\\ \Delta_{13}+\Delta_{31}\\ e^{-i(\pi/3)}\Delta_{22}+e^{i(\pi/3)}\Delta_{44}\\ e^{-i(\pi/3)}\Delta_{22}-e^{i(\pi/3)}\Delta_{44}\\ \Delta_{24}+\Delta_{42}\end{pmatrix},$$

$$\Pi_2=\begin{pmatrix} e^{-i(\pi/3)}\Delta_{12}+e^{i(\pi/3)}\Delta_{34}\\ e^{-i(\pi/3)}\Delta_{12}-e^{i(\pi/3)}\Delta_{34}\\ \Delta_{14}-\Delta_{32}\\ e^{-i(\pi/3)}\Delta_{21}+e^{i(\pi/3)}\Delta_{43}\\ e^{-(i\pi/3)}\Delta_{21}-e^{i(\pi/3)}\Delta_{43}\\ \Delta_{41}-\Delta_{23}\end{pmatrix},$$

$$\Omega_1=\begin{pmatrix}\Delta_{13}-\Delta_{31}\\ \Delta_{24}-\Delta_{42}\end{pmatrix},\quad \Omega_2=\begin{pmatrix}\Delta_{14}+\Delta_{32}\\ \Delta_{41}+\Delta_{23}\end{pmatrix}.$$

Under a space-group symmetry operation S, they transform in the following way:

$$\Pi_i\rightarrow A_S(\Pi_i)\Pi_i\quad\text{and}\quad \Omega_i\rightarrow B_S(\Omega_i)\Omega_i,$$

where $A_S(\Pi_i)$ $[B_S(\Omega_i)]$ is the 6×6 (2×2) matrix representing the symmetry operation S, whose detailed expressions are displayed in Appendix C.

Since the pairing amplitude Δ_{ij} is not a gauge invariant object, we have to look into the symmetry of the bilinears such as $D_{ij,kl}\equiv\Delta_{ij}^\dagger\Delta_{kl}$. Even though the number of all possible tensors $D_{ij,kl}$ is very large, we can reduce the complexity of the symmetry analysis by focusing on the objects carrying the momentum compatible with the $\sqrt{3}\times\sqrt{3}$ ordering. This idea leads us to exclude $D_{ij,kl}$ made of the basis Π_2 and Ω_2. In addition, Π_1 and Ω_1 have opposite spin parities, that is, Π_1 is spin singlet while Ω_1 is spin triplet. Therefore all we have to consider are the terms like $\Pi_1^\dagger\mathrm{M}_\Pi\Pi_1$ and $\Omega_1^\dagger\mathrm{M}_\Omega\Omega_1$.

First, we define a set of Pauli matrices τ_i acting on the space spanned by Ω_1. Using the transformation properties of Ω_1 under the space group, we obtain a pair $(\Omega_1^\dagger\tau_x\Omega_1,\Omega_1^\dagger\tau_y\Omega_1)$ which has the momentum $\mathbf{K}=(\frac{2\pi}{3},0)$ and transforms as the E_3 irreducible representation of the enlarged point group, $G_{P,\mathbf{b}}$.

To understand the symmetry of $\Pi_1^\dagger\mathrm{M}_\Pi\Pi_1$, we introduce a set of the Gell-Mann matrices λ_a $(a=1,\ldots,8)$ (Ref. 53) as well as the Pauli matrices τ_i. For convenience, we also define the matrix, $\lambda_9=\sqrt{\frac{2}{3}}\mathbf{I}_3$, where $\mathbf{I}_3$ is the 3×3 identity matrix. The Gell-Mann matrices are acting on the space spanned by either $(\Pi_{1,1},\Pi_{1,2},\Pi_{1,3})$ or $(\Pi_{1,4},\Pi_{1,5},\Pi_{1,6})$ and τ_i connects these two three-component vectors. Here $\Pi_{1,n}$ indicates the nth component of Π_1.

We have examined the symmetry of all possible bilinears $\Pi_1^\dagger\mathrm{M}_\Pi\Pi_1$ and found out that there are only two sets of bilinears which have the momentum $\mathbf{K}$ compatible with the $\sqrt{3}\times\sqrt{3}$ ordering. These are given by

$$\mathbf{X}_{E_3}=\begin{pmatrix}\frac{2\sqrt{2}}{3}\Pi_1^\dagger\tau_1\lambda_8\Pi_1+\frac{1}{3}\Pi_1^\dagger\tau_1\lambda_9\Pi_1\\ \frac{2\sqrt{2}}{3}\Pi_1^\dagger\tau_2\lambda_8\Pi_1+\frac{1}{3}\Pi_1^\dagger\tau_2\lambda_9\Pi_1\end{pmatrix},$$

$$\mathbf{X}_Q=\begin{pmatrix}\Pi_1^\dagger\tau_1\lambda_3\Pi_1\\ \frac{1}{3}\Pi_1^\dagger\tau_1\lambda_8\Pi_1-\frac{2\sqrt{2}}{3}\Pi_1^\dagger\tau_1\lambda_9\Pi_1\\ \Pi_1^\dagger\tau_2\lambda_3\Pi_1\\ \frac{1}{3}\Pi_1^\dagger\tau_2\lambda_8\Pi_1-\frac{2\sqrt{2}}{3}\Pi_1^\dagger\tau_2\lambda_9\Pi_1\end{pmatrix}.$$

In the above $\mathbf{X}_{E_3}$ transforms as the two-dimensional E_3 irreducible representation of the enlarged point group $G_{P,\mathbf{b}}$. On the other hand $\mathbf{X}_Q$ constitutes a basis of the four-dimensional Q irreducible representation. Therefore the in-

stability given by $\mathbf{X}_{E_3}$ has the symmetry consistent with the $\sqrt{3}\times\sqrt{3}$ orders which we have discussed in detail in previous sections.

Since we are considering an instability from a gapped phase, to stabilize the resulting ordered state, the condensation energy should be larger than the excitation gap. However, because the magnitude of the energy gap reduces as J_t/J_e increases, the instability can occur beyond the critical value of J_t/J_e. Finally, since the condition of $\langle \mathbf{X}_{E_3}\rangle \neq 0$ does not constrain the magnitude of $\langle \Pi_1\rangle$, $\langle \Pi_1\rangle$ can have both zero and nonzero values. If $\langle \Pi_1\rangle \neq 0$ with $\langle \mathbf{X}_{E_3}\rangle \neq 0$, we have Z_2 spin liquid supporting fractionalized quasiparticles and breaking the translational symmetry at the same time. This state is similar to the Amperean paired state,[54] which is recently suggested as a possible ground state of the organic compound κ-(BEDT-TTF)$_2$Cu$_2$(CN)$_3$. On the other hand, if $\langle \Pi_1\rangle = 0$ while $\langle \mathbf{X}_{E_3}\rangle \neq 0$, we have more conventional phase transforming as an E_3 irreducible representation.

In conclusion, the symmetry analysis of the low-energy fermions near the conduction-band minima shows that the instability of the SL$[0,0,\pi]$ state from the particle-particle channel supports valence-bond solid phases, which have the $\sqrt{3}\times\sqrt{3}$ unit cell transforming as E_3 irreducible representations of the enlarged point group $G_{P,\mathbf{b}}$. Remember that the J_e-dimer VBS phase is induced via the monopole condensation from the SL$[0,0,\pi]$ state for small J_t/J_e limit. Therefore we can obtain the valence-bond solid ground states both for $J_t/J_e \ll 1$ and $J_t/J_e \gg 1$ limits from the instability of the SL$[0,0,\pi]$ state.

C. Projected wave-function approach

We next assess the stability of the SL$[0,0,\pi]$ spin liquid toward columnar dimer order in the Guzwiller projected state. In order to do this, we include a parameter δt in the mean-field Hamiltonian which corresponds to strengthening the fermion hopping on those bonds which dimerize in the classical columnar dimer state, shown in Fig. 11(a), and Gutzwiller project the resulting state. Clearly, if $\delta t \gg 1$, the resulting wave function will be precisely the classical columnar dimer pattern. The energy change in the weakly distorted state as a function of the distortion parameter δt serves as a measure of the inverse susceptibility of the SL$[0,0,\pi]$ state toward columnar dimer order. As seen from Fig. 20, the SL$[0,0,\pi]$ state is stable, with a positive inverse susceptibility, for $J_t/J_e \lesssim 2$, but is unstable, with a negative inverse susceptibility for $J_t/J_e \gtrsim 2$. Further, the optimal δt appears to increase continuously for $J_t/J_e \gtrsim 2$. This suggests that the SL$[0,0,\pi]$ state possibly undergoes a continuous transition into a state with $\sqrt{3}\times\sqrt{3}$ columnar dimer order at $J_t/J_e \approx 2.0$. We discuss the phase transition more carefully in the next section.

VI. PHASE TRANSITION BETWEEN VBS PHASES

The results in previous sections show that there is a phase transition between the J_e-dimer VBS phase and the columnar 18-site VBS phase with increasing J_t/J_e. To describe the phase transition between these two VBS phases, we con-

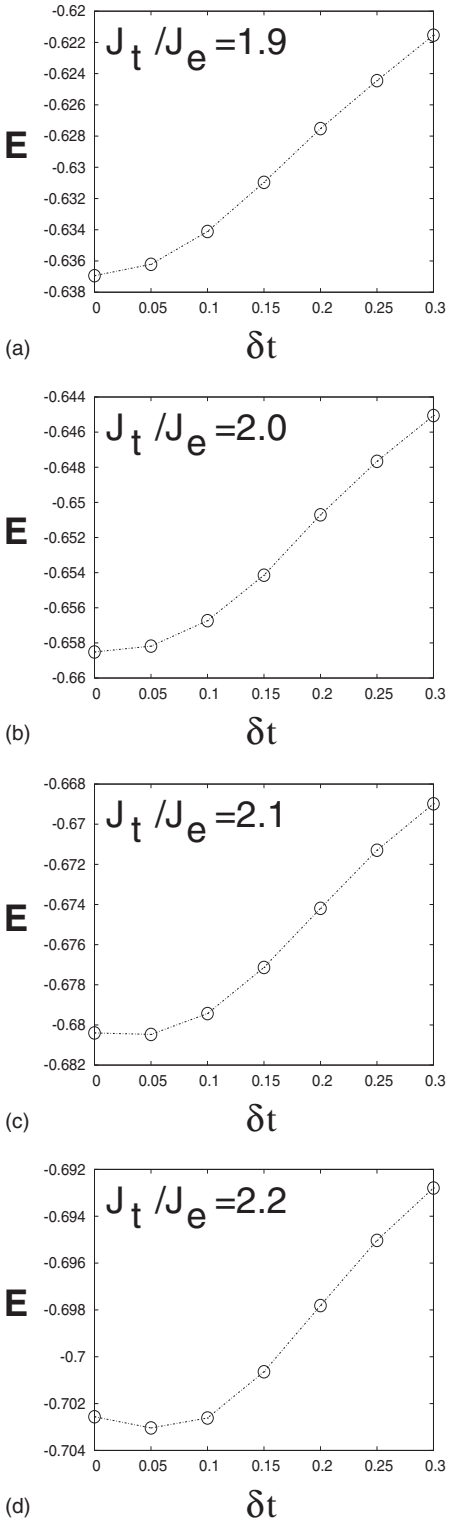

FIG. 20. Change in energy of the Gutzwiller projected SL$[0,0,\pi]$ spin liquid state upon including a distortion δt corresponding to increased fermion hopping amplitude on the dimerized bonds of the $\sqrt{3}\times\sqrt{3}$ columnar dimer state shown in Fig. 11(a). For $J_t/J_e = 1.9, 2.0$, the SL$[0,0,\pi]$ state is found to be stable against this distortion, while it is seen to be unstable for $J_t/J_e = 2.1, 2.2$. (This calculation was carried out on a system with 12×12 unit cells, i.e., with 864 spins. The statistical errors on the computed energy are of the order of the symbol size.)

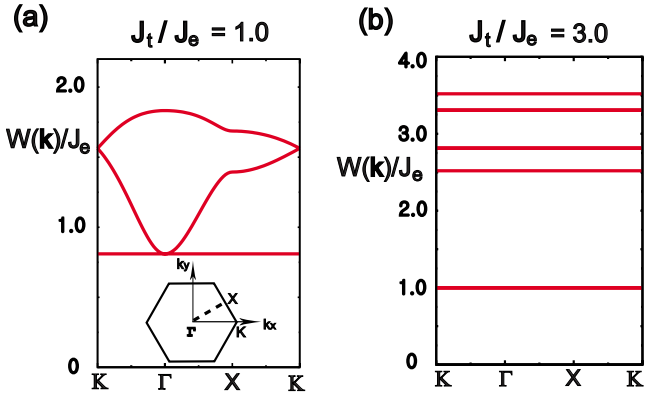

FIG. 21. (Color online) Triplet dispersions of valence-bond solid ground states along high-symmetry directions of the Brillouin zone. The dispersions are obtained from the self-consistent bond operator mean-field theory. (a) Triplet dispersion of the J_e-dimer VBS phase for $J_t/J_e=1$. (b) Triplet dispersion of the columnar 18-site VBS phase for $J_t/J_e=3$.

struct a Landau-Ginzburg free energy introducing a two-component vector (Φ_1,Φ_2), which transforms as an E_3 irreducible representation of the enlarged point group $G_{P,\mathbf{b}}$. Since the VBS phases are time-reversal invariant, we can use two real numbers, Φ_1 and Φ_2. The Landau-Ginzburg free energy can be written using all possible invariants made of Φ_1 and Φ_2. In particular, it is important to note that there is a third-order invariant, which belongs to the A_1 irreducible representation of the following decomposition:

$$E_3 \otimes E_3 \otimes E_3 = A_1 \oplus B_1 \oplus 3E_3. \tag{25}$$

In terms of Φ_1 and Φ_2, the third-order invariant is given by $\Phi_2(3\Phi_1^2-\Phi_2^2)$. Straightforward extension of the same group theoretical analysis to quartic order shows that there is only one quartic invariant of $(\Phi_1^2+\Phi_2^2)^2$. Collecting all invariants up to quartic order, the Landau-Ginzburg free-energy density is written as

$$f = \alpha(\Phi_1^2+\Phi_2^2) + \lambda\Phi_2(3\Phi_1^2-\Phi_2^2) + u(\Phi_1^2+\Phi_2^2)^2. \tag{26}$$

For convenience we define a complex variable Φ as follows:

$$\Phi \equiv \Phi_2 - i\Phi_1 \equiv |\Phi|e^{i\theta}. \tag{27}$$

Then the free-energy density is given by

$$f = \alpha|\Phi|^2 + u|\Phi|^4 - \lambda|\Phi|^3\cos(3\theta). \tag{28}$$

Given $u>0$ and $\lambda>0$, the above mean-field free energy predicts two different phases separated by a first-order transition point at $\alpha=\alpha_c=\lambda^2/(4\mu)$. For $\alpha>\alpha_c$, we have a disordered phase with $|\Phi|=0$. On the other hand, ordered phases with $|\Phi|\neq 0$ and $\theta=\frac{2\pi n}{3}$ $(n=0,1,2)$ appear when $\alpha<\alpha_c$. The three ordered states describe the threefold degenerate VBS phases with $\sqrt{3}\times\sqrt{3}$ pattern.

Considering slow spatial variation in Φ, the Euclidean Landau-Ginzburg effective action is given by

$$S = \int d^3x\{|\partial_\mu\Phi|^2 + \alpha|\Phi|^2 + u|\Phi|^4 - \lambda|\Phi|^3\cos(3\theta)\}. \tag{29}$$

The above effective action is nothing but the action for the three-dimensional Z_3-clock model. Previous Monte Carlo simulations suggest that the phase transition associated with the Z_3 symmetry breaking is weakly first order.[55–57] The wave-function numerics in the previous section, however, are not inconsistent with this scenario considering the small system size. In addition, the nature of the transition may not have been completely settled.[58]

VII. TRIPLON DISPERSION IN THE VBS STATES

In Fig. 21, we plot the triplet dispersions of the two VBS phases, which are obtained from the bond operator mean-field theory. The triplet dispersion of the J_e-dimer VBS state is shown in Fig. 21(a). Since the unit cell of the J_e-dimer VBS state is composed of three dimers, we have three triplet modes in the spectrum. Here we neglect the fact that each triplet particle has three components (x, y, and z) when we count the number of bands. Interestingly, the lowest band is flat and touches another dispersive band at the Brillouin-zone center. The emergence of this band touching has a topological origin.[37,59] The flatband reflects the existence of localized eigenstates. In fact, there are two different types of localized eigenstates. The first set is given by states which are confined within dodecagons. Each dodecagon supports a single localized eigenstate. In addition, there are "noncontractible" loop states constituting the second group of localized eigenstates. In contrast to the states confined within dodecagons, these loop states extend over the whole lattice system one dimensionally. The topological characteristics of these loop states can be easily understood using the periodic boundary condition, under which a two-dimensional system has a torus geometry. In this situation, there are two independent loop states winding the torus once. Since these states cannot be shrunk to points, they are noncontractible. Counting the number of independent localized states carefully, we see that the number of degenerate localized eigenstates is larger than the number of dimers on the lattice.[37,59] It means that a single flatband is not enough to support all independent localized eigenstates. Therefore additional degrees of freedom must be provided by another band, leading to the band touching.

The triplet dispersion of the columnar 18-site VBS state is displayed in Fig. 21(b). We have nine triplet bands which are all flat within our mean-field approach. The degeneracies of the flatbands are given by 3, 1, 2, 2, and 1 counting from the bottom to the top bands. In contrast to the case of the J_e-dimer VBS phase, the flat structure emerges simply because the dimers on expanded links are completely decoupled from those on neighboring perfect dodecagons. The lowest flatband is triply degenerate, which comes from the three dimers on expanded links. The remaining six dimers of the unit cell lying on perfect dodecagons constitute the other six bands with higher energies. Therefore we expect that the nature of the valence-bond solid ground states can be dem-

onstrated via neutron-scattering experiments measuring triplet dispersion spectra.

VIII. DISCUSSION

In summary, we have shown that the ground state of the nearest-neighbor Heisenberg model on the star lattice undergoes a phase transition from "the J_e-dimer VBS phase" which respects all lattice symmetries to "the columnar 18-site VBS phase" which exhibits $\sqrt{3}\times\sqrt{3}$ order with increasing J_t/J_e. From the Landau-Ginzburg analysis, this appears to be a conventional quantum phase transition which is described as the thermal transition of the $2+1$-dimensional Z_3-clock model.

If $S=1/2$ variants of the organic Iron-Acetate magnet can be synthesized, they would be particularly good candidates to study the phase diagram discussed in this paper since it may be possible to pressure tune the ratio J_t/J_e significantly in such systems. Both VBS states obtained here would exhibit a spin gap in uniform susceptibility measurements. We expect a direct signature of the 18-site VBS order to appear in x-ray scattering or neutron diffraction studies which would see a change in the crystal periodicity. Ignoring coupling to phonons, the 18-site VBS state should exhibit a thermal transition in the universality class of the Z_3-clock model in $D=2$ dimensions. In addition, the two VBS phases exhibit quite distinct behaviors in their triplet excitation spectra as discussed above which could be tested using inelastic neutron-scattering experiments.

ACKNOWLEDGMENTS

We thank Daniel Podolsky, Tingpong Choy, Fa Wang, and Jason Alicea for helpful discussions. This work was supported by the NSERC, the Canada Research Chair Program, and the Canadian Institute for Advanced Research. A.P. acknowledges support from the Sloan Foundation, the Connaught Foundation and an Ontario ERA.

APPENDIX A: DERIVATION OF THE LOW-ENERGY EFFECTIVE HAMILTONIANS

Here we present the details of how we have derived the low-energy effective Hamiltonians of the spin liquid states discussed in Sec. II B.

1. Effective Hamiltonian for SL$[\frac{\pi}{2},\frac{\pi}{2},\pi]$

For the gauge choice depicted in Fig. 5(a), the mean-field Hamiltonian corresponding to the SL$[\frac{\pi}{2},\frac{\pi}{2},\pi]$ can be written in momentum space as

$$H_{\mathrm{MF}}=-J_t\chi_t\sum_{\mathbf{k}}\sum_{m,n}f^{\dagger}_{\mathbf{k},m}H(\mathbf{k})_{m,n}f_{\mathbf{k},n}, \tag{A1}$$

in which

$$H(\mathbf{k})=\begin{pmatrix} 0 & i & i & \lambda z_2^* & 0 & 0\\ -i & 0 & -i & 0 & \lambda & 0\\ -i & i & 0 & 0 & 0 & \lambda z_1^*\\ \lambda z_2 & 0 & 0 & 0 & -i & -i\\ 0 & \lambda & 0 & i & 0 & -i\\ 0 & 0 & \lambda z_1 & i & i & 0 \end{pmatrix},$$

where $z_1=e^{i\mathbf{k}\cdot\mathbf{a}_1}$ and $z_2=e^{i\mathbf{k}\cdot\mathbf{a}_2}$. m, n are indices for the six sites inside a unit cell and $\lambda=J_e\chi_e/J_t\chi_t$. The indices for the spin quantum number are dropped for simplicity. Here we define the Fourier transformation via $f_{\mathbf{R},n}=\frac{1}{\sqrt{N_c}}\Sigma_{\mathbf{k}}e^{i\mathbf{k}\cdot\mathbf{R}}f_{\mathbf{k},n}$.

As described in Fig. 6(b), the conduction (valence) band shows the dispersion minimum (maximum) at the momentum $\pm\mathbf{Q}$. The energy eigenvalues of $H(\mathbf{k})$ at $\mathbf{k}=\pm\mathbf{Q}$ are given by

$$E_1^{\pm}=\sqrt{3/2+\lambda^2-1/2\sqrt{9+12\lambda^2}},$$

$$E_2^{\pm}=-E_1^{\pm}, \tag{A2}$$

where $\pm$ indicates the two momentum position $\pm\mathbf{Q}$ and 1 and 2 represent the conduction (1) and valence (2) bands, respectively. To make the analytic treatment of the problem possible we focus on the small λ limit. Note that the overall spinon band structure does not change upon varying λ. Expanding the energy eigenvalues in powers of λ, we get

$$E_1^{\pm}=-E_2^{\pm}\approx\frac{1}{\sqrt{3}}\lambda^2+O(\lambda^4).$$

The corresponding eigenvectors are

$$(\nu_1^+)^T=\frac{e^{-i(\pi/6)}}{\sqrt{3(1+b^2)}}\left\{-1-\frac{1}{3}\lambda^2,-1-\frac{1}{3}\lambda^2,1+\frac{1}{3}\lambda^2,-\frac{1}{\sqrt{3}}\lambda e^{i(\pi/3)},-\frac{1}{\sqrt{3}}\lambda,\frac{1}{\sqrt{3}}\lambda e^{i(2\pi/3)}\right\},$$

$$(\nu_2^+)^T=\frac{e^{i(\pi/6)}}{\sqrt{3(1+b^2)}}\left\{-\frac{1}{\sqrt{3}}\lambda e^{-i(\pi/3)},\frac{1}{\sqrt{3}}\lambda,-\frac{1}{\sqrt{3}}\lambda e^{-i(2\pi/3)},1+\frac{1}{3}\lambda^2,-1-\frac{1}{3}\lambda^2,1+\frac{1}{3}\lambda^2\right\},$$

$$(\nu_1^-)^T=\frac{e^{-i(2\pi/3)}}{\sqrt{3(1+b^2)}}\left\{\frac{1}{\sqrt{3}}\lambda e^{i(\pi/3)},-\frac{1}{\sqrt{3}}\lambda,\frac{1}{\sqrt{3}}\lambda e^{i(2\pi/3)},1+\frac{1}{3}\lambda^2,-1-\frac{1}{3}\lambda^2,1+\frac{1}{3}\lambda^2\right\},$$

$$(\nu_2^-)^T = \frac{e^{i(2\pi/3)}}{\sqrt{3(1+b^2)}}\left\{-1-\frac{1}{3}\lambda^2,-1-\frac{1}{3}\lambda^2,1 + \frac{1}{3}\lambda^2,\frac{1}{\sqrt{3}}\lambda e^{-(i\pi/3)},\frac{1}{\sqrt{3}}\lambda,-\frac{1}{\sqrt{3}}\lambda e^{-i(2\pi/3)}\right\}, \quad \text{(A3)}$$

where the superscript T means taking transposition. The above eigenvalues and eigenvectors satisfy $H(\pm\mathbf{Q})\nu_\alpha^\pm = E_\alpha^\pm \nu_\alpha^\pm$ ($\alpha=1$ and 2) correctly up to the third order in λ.

Now we want to construct the effective Hamiltonian describing the states which have small momentum deviation from $\pm\mathbf{Q}$, i.e., states with $\mathbf{k}=\pm\mathbf{Q}+\mathbf{q}$. We first define $\Delta H(\mathbf{q}) \equiv H(\pm\mathbf{Q}+\mathbf{q}) - H(\pm\mathbf{Q})$. Keeping terms which are first order in $\mathbf{q}$ and projecting them into the low-energy space spanned by the eigenvectors $\nu_\alpha^\pm$ ($\alpha=1,2$), we obtain the following effective Hamiltonian:

$$H^\pm(\mathbf{q}) \equiv H(\pm\mathbf{Q}+\mathbf{q}) = -\frac{\lambda}{\sqrt{3}}(q_x\tau_x + q_y\tau_y) + \frac{\lambda^2}{\sqrt{3}}\tau_z.$$

Finally, defining the continuum fermion fields using the spinon variables as

$$[\psi_\pm(\mathbf{q})]^T \sim [\sum_{n=1}^{6} (\nu_1^\pm)_n^* f_{\pm\mathbf{Q}+\mathbf{q},n}, \sum_{n=1}^{6} (\nu_2^\pm)_n^* f_{\pm\mathbf{Q}+\mathbf{q},n}],$$

$$[\Psi(\mathbf{q})]^T \equiv \{[\psi_+(\mathbf{q})]^T, [\psi_-(\mathbf{q})]^T\}, \quad \text{(A4)}$$

we arrive at the low-energy effective Hamiltonian written in Eq. (14) which is nothing but the Hamiltonian for the massive Dirac particles.

2. Effective Hamiltonian for SL$[-\frac{\pi}{2},\frac{\pi}{2},0]$

The low-energy Hamiltonian corresponding to the SL$[-\frac{\pi}{2},\frac{\pi}{2},0]$ can be obtained following the similar steps used to construct the massive Dirac Hamiltonian of the SL$[\frac{\pi}{2},\frac{\pi}{2},\pi]$. Adopting the flux configuration depicted in Fig. 5(b), we have an electron pocket centered at the momentum $\mathbf{K}$ and an hole pocket centered at the momentum $-\mathbf{K}$. At each momentum $\pm\mathbf{K}$ there is a linear band touching as is shown in Fig. 5(b). The energy eigenvalues of the degenerate states at $\mathbf{k}=\pm\mathbf{K}$ are given by

$$E^+ = \frac{\sqrt{3+\lambda^2}-\sqrt{3}}{2} \approx \frac{1}{\sqrt{3}}\lambda^2 + O(\lambda^4),$$

$$E^- = -E^+ \approx -\frac{1}{\sqrt{3}}\lambda^2 + O(\lambda^4),$$

where E^+ (E^-) represents the degenerate energy eigenvalue at the momentum $\mathbf{K}$ ($-\mathbf{K}$). We choose the corresponding eigenvectors in the following way:

$$(\nu_1^+)^T = \frac{e^{i(\pi/3)}}{\sqrt{3(1+b^2)}}\left\{-\frac{1}{\sqrt{3}}\lambda e^{-i(2\pi/3)},-\frac{1}{\sqrt{3}}\lambda,\frac{1}{\sqrt{3}}\lambda e^{i(2\pi/3)},-1 - \frac{1}{3}\lambda^2,-1-\frac{1}{3}\lambda^2,1+\frac{1}{3}\lambda^2\right\},$$

$$(\nu_2^+)^T = \frac{e^{-(i\pi/3)}}{\sqrt{3(1+b^2)}}\left\{-1-\frac{1}{3}\lambda^2,-1-\frac{1}{3}\lambda^2,1+\frac{1}{3}\lambda^2, -\frac{1}{\sqrt{3}}\lambda e^{i(2\pi/3)},-\frac{1}{\sqrt{3}}\lambda,\frac{1}{\sqrt{3}}\lambda e^{-i(2\pi/3)}\right\},$$

$$(\nu_1^-)^T = \frac{e^{-(i\pi/6)}}{\sqrt{3(1+b^2)}}\left\{-1-\frac{1}{3}\lambda^2,-1-\frac{1}{3}\lambda^2,1 + \frac{1}{3}\lambda^2,\frac{1}{\sqrt{3}}\lambda e^{-i(2\pi/3)},\frac{1}{\sqrt{3}}\lambda,-\frac{1}{\sqrt{3}}\lambda e^{i(2\pi/3)}\right\},$$

$$(\nu_2^-)^T = \frac{e^{i(\pi/6)}}{\sqrt{3(1+b^2)}}\left\{\frac{1}{\sqrt{3}}\lambda e^{i(2\pi/3)},\frac{1}{\sqrt{3}}\lambda,-\frac{1}{\sqrt{3}}\lambda e^{-i(2\pi/3)},-1 - \frac{1}{3}\lambda^2,-1-\frac{1}{3}\lambda^2,1+\frac{1}{3}\lambda^2\right\}, \quad \text{(A5)}$$

satisfying $H(\pm\mathbf{K})\nu_\alpha^\pm = E^\pm\nu_\alpha^\pm$ ($\alpha=1$ and 2) correctly up to the third order in λ. The first-order perturbation theory combined with the projection into the low-energy space spanned by $\nu_\alpha^\pm$ ($\alpha=1$, 2) leads to the following Hamiltonian:

$$H^\pm(\mathbf{q}) \equiv H(\pm\mathbf{K}+\mathbf{q}) = -\frac{\lambda}{\sqrt{3}}(q_x\tau_x + q_y\tau_y) + \frac{\lambda^2}{\sqrt{3}}\mu_z.$$

Using the continuum fermion field defined in Eq. (A4) we obtain the low-energy effective Hamiltonian displayed in Eq. (15).

3. Effective Hamiltonian for SL [0,0,0]

The mean-field band structure of the SL [0,0,0] has a flat-band lying at the Fermi energy, which is touching a dispersive band at the zone center, i.e., at the momentum $\mathbf{\Gamma}=(0,0)$. To describe the low-energy states near the $\mathbf{\Gamma}$ point, we use the degenerate perturbation theory again. However, since the two bands touch quadratically, we keep the perturbation expansion up to the quadratic order in momentum. For the SL [0,0,0], the mean-field Hamiltonian is given by

$$H_{\mathrm{MF}} = -J_t\chi_t \sum_{\mathbf{k}} \sum_{m,n} f_{\mathbf{k},m}^\dagger H(\mathbf{k})_{m,n} f_{\mathbf{k},n}, \quad \text{(A6)}$$

in which

$$H(\mathbf{k}) = \begin{pmatrix} 0 & 1 & 1 & \lambda z_2^* & 0 & 0 \\ 1 & 0 & 1 & 0 & \lambda & 0 \\ 1 & 1 & 0 & 0 & 0 & \lambda z_1^* \\ \lambda z_2 & 0 & 0 & 0 & 1 & 1 \\ 0 & \lambda & 0 & 1 & 0 & 1 \\ 0 & 0 & \lambda z_1 & 1 & 1 & 0 \end{pmatrix}.$$

We divide $H(\mathbf{k})$ into two pieces such that $H(\mathbf{k})=H_0+V$ in which $H_0 \equiv H(\mathbf{k}=0)$. Diagonalization of H_0 gives the eigenvalues $E_0=\{-1-\lambda,-1-\lambda,-1+\lambda,-1+\lambda,2-\lambda,2+\lambda\}$. Note that there are two pairs of doubly degenerate eigenvalues. Here we focus on one of the degenerate eigenvalues $w_0=-1+\lambda$ which is lying at the Fermi level. We choose the

following two degenerate eigenvectors corresponding to w_0:

$$(\nu_1)^T = \frac{1}{\sqrt{12}}\{2,-1,-1,2,-1,-1\},$$

$$(\nu_2)^T = \frac{1}{\sqrt{4}}\{0,1,-1,0,1,-1\}.$$

Now we introduce the projection operator $\hat{P}_0$ ($\hat{P}_1$) which projects states into (out of) the low-energy space spanned by ν_1 and ν_2. That is, $\hat{P}_0 = \nu_1 \cdot \nu_1^\dagger + \nu_2 \cdot \nu_2^\dagger$ and $\hat{P}_1 = \hat{I} - \hat{P}_0$. We also define $V_0 \equiv \hat{P}_0 V \hat{P}_0$ and $V_1 \equiv V - V_0$. Then $H(\mathbf{k}) = H_0 + V_0 + V_1$. The projected Hamiltonian is given by[60]

$$H_{P_0}(\mathbf{k}) \equiv \hat{P}_0 H(\mathbf{k}) \hat{P}_0 \approx \hat{P}_0[H_0 + V_0]\hat{P}_0 + \hat{P}_0 V_1 \hat{P}_1 \frac{1}{w_0 - H_0} \hat{P}_1 V_1 \hat{P}_0, \tag{A7}$$

which is valid up to the quadratic order in $\mathbf{k}$. The resulting Hamiltonian can be written as

$$H_{P_0}(\mathbf{k}) = \frac{\lambda}{2\lambda - 3} \begin{pmatrix} k_y^2 & -k_x k_y \\ -k_x k_y & k_x^2 \end{pmatrix}.$$

We define the continuum fields as

$$(\psi(\mathbf{k}))^T \sim \{\sum_{n=1}^{6} (\nu_1^{\pm})_n^* f_{\mathbf{k},n}, \sum_{n=1}^{6} (\nu_2^{\pm})_n^* f_{\mathbf{k},n}\}. \tag{A8}$$

Finally, combining the above results we obtain the following low-energy effective Hamiltonian:

$$H_{\text{eff}} = \frac{1}{m_{\text{eff}}} \int \frac{d^2\mathbf{k}}{(2\pi)^2} \psi^\dagger(\mathbf{k}) h_{\text{eff}}(\mathbf{k}) \psi(\mathbf{k}),$$

in which

$$h_{\text{eff}}(\mathbf{k}) = (k_x^2 + k_y^2)\tau_0 - (k_x^2 - k_y^2)\tau_z - 2k_x k_y \tau_x.$$

APPENDIX B: SYMMETRY AND CONTINUUM FIELD OF THE SL[$-\frac{\pi}{2}, \frac{\pi}{2}, 0$] STATE

In this section we show how the continuum fields of the SL[$-\frac{\pi}{2}, \frac{\pi}{2}, 0$] state transform under the microscopic symmetries of the lattice. Here we follow the procedures suggested by Hermele *et al.* in Ref. 10. To obtain the necessary information we consider a finite system with periodic boundary conditions in both $\mathbf{a}_1$ and $\mathbf{a}_2$ directions. In particular, to determine how the wave functions at the momentum $\pm\mathbf{K}$ (we call it as the nodal wave functions) transform under the space-group symmetries of the Ansatz, we consider the 3×3 lattice system, that is, the system is periodic under the translation by $3\mathbf{a}_1$ and $3\mathbf{a}_2$. Since a unit cell (indexed by a vector $\mathbf{R}$) contains six sites labeled by n, the finite system consists of 54 sites. The nine points within the Brillouin zone of the finite system contain the nodal points $\pm\mathbf{K}$ and respect all the point-group symmetries of the Ansatz.

Using the eigenvectors ν_α^a (a=+,− and α=1,2) in Eq. (A5), the nodal wave function is given by

$$\Phi_{a,\alpha}(\mathbf{R},n) = \frac{e^{i\mathbf{a}\mathbf{K}\cdot\mathbf{R}}(\nu_\alpha^a)_n}{3}.$$

Then the continuum field is written as

$$\Psi_{a,\alpha}(\mathbf{q}=0) = \sum_{\mathbf{R},n} \Phi_{a,\alpha}^*(\mathbf{R},n) f_{\mathbf{R},n}.$$

Now we consider a symmetry operation S under which the spinons transform as

$$S: f_{\mathbf{i},\sigma} \to G_S(\mathbf{i}) f_{S(\mathbf{i}),\sigma}.$$

In particular we consider the following symmetry operations:

(i) The $\mathbf{a}_1$ translation (T_1);

$$T_1: f_{\mathbf{R},n,\sigma} \to G_{T_1}(\mathbf{R},n) f_{\mathbf{R}+\mathbf{a}_1,n,\sigma}.$$

(ii) The $\mathbf{a}_2$ translation (T_2);

$$T_2: f_{\mathbf{R},n,\sigma} \to G_{T_2}(\mathbf{R},n) f_{\mathbf{R}+\mathbf{a}_2,n,\sigma}.$$

(iii) The $\frac{2\pi}{3}$ rotation ($C_{2\pi/3}$);

$$C_{2\pi/3}: f_{\mathbf{R},n,\sigma} \to G_{C_{2\pi/3}}(\mathbf{R},n) f_{C_{2\pi/3}(\mathbf{R},n),\sigma}.$$

(iv) The y reflection (R_y);

$$R_y: f_{(x,y),n,\sigma} \to G_{R_y}(\mathbf{R},n) f_{(x,-y),m,\sigma},$$

where $\mathbf{R}=(x,y)$ and $(n,m) \in \{(1,4),(2,6),(3,5),(4,1),(5,3),(6,2)\}$.

(v) Time-reversal and inversion ($T \cdot I$);

$$T \cdot I: f_{\mathbf{R},n,\sigma} \to (i\sigma_2)_{\sigma,\sigma'} f_{-\mathbf{R},(n+3),\sigma'},$$

in which (n+3) represents the remainder when it is divided by six.

(vi) Charge conjugation (C^*);

$$C_*: f_{\mathbf{R},n,\sigma} \to \epsilon_n f_{\mathbf{R},n,\sigma}^\dagger,$$

in which $\epsilon_i = 1$ for i=1,2,3 and −1 otherwise.

For each of the symmetry operation S, the matrix representation of the symmetry S is defined as

$$(S)_{S(\mathbf{i}),\mathbf{i}} \equiv G_S(\mathbf{i}).$$

The action of the symmetry operation S on the nodal wave function is given by $S\Phi_a = c_{ab}\Phi_b$. Now a and b denote the nodal and the two-component Dirac indices collectively. Finally, the transformation of the nodal wave function reflects the action of S on the continuum field such as

$$S: \Psi_a \to c_{ab}^* \Psi_b.$$

The transformation rule of the continuum field under all the above symmetry operations is summarized in Eq. (16).

APPENDIX C: EXPRESSIONS OF THE MATRICES $A_S(\Pi_i)$ AND $B_S(\Omega_i)$

Here we present the expressions of the matrices $A_S(\Pi_i)$ and $B_S(\Omega_i)$ ($S = T_{a_1}$, T_{a_2}, R_y, and $C_{\pi/3}$), which are defined in Sec. V B. At first $A_S(\Pi_1)$ are given by

$$A_{T_{a_1}}(\Pi_1):\begin{pmatrix} e^{i(2\pi/3)} & 0 & 0 & 0 & 0 & 0 \\ 0 & e^{-i(\pi/3)} & 0 & 0 & 0 & 0 \\ 0 & 0 & e^{-i(\pi/3)} & 0 & 0 & 0 \\ 0 & 0 & 0 & e^{-i(2\pi/3)} & 0 & 0 \\ 0 & 0 & 0 & 0 & e^{i(\pi/3)} & 0 \\ 0 & 0 & 0 & 0 & 0 & e^{i(\pi/3)} \end{pmatrix},$$

$$A_{T_{a_2}}(\Pi_1):\begin{pmatrix} e^{i(\pi/3)} & 0 & 0 & 0 & 0 & 0 \\ 0 & e^{i(\pi/3)} & 0 & 0 & 0 & 0 \\ 0 & 0 & e^{-i(2\pi/3)} & 0 & 0 & 0 \\ 0 & 0 & 0 & e^{-i(\pi/3)} & 0 & 0 \\ 0 & 0 & 0 & 0 & e^{-i(\pi/3)} & 0 \\ 0 & 0 & 0 & 0 & 0 & e^{i(2\pi/3)} \end{pmatrix},$$

$$A_{R_y}(\Pi_1):\begin{pmatrix} 1 & 0 & 0 & 0 & 0 & 0 \\ 0 & 0 & 1 & 0 & 0 & 0 \\ 0 & 1 & 0 & 0 & 0 & 0 \\ 0 & 0 & 0 & 1 & 0 & 0 \\ 0 & 0 & 0 & 0 & 0 & -1 \\ 0 & 0 & 0 & 0 & -1 & 0 \end{pmatrix},$$

$$A_{C_{\pi/3}}(\Pi_1):\begin{pmatrix} 0 & 0 & 0 & 0 & 0 & 1 \\ 0 & 0 & 0 & 1 & 0 & 0 \\ 0 & 0 & 0 & 0 & i & 0 \\ 0 & 0 & 1 & 0 & 0 & 0 \\ -1 & 0 & 0 & 0 & 0 & 0 \\ 0 & i & 0 & 0 & 0 & 0 \end{pmatrix}.$$

Similarly for $A_S(\Pi_2)$,

$$A_{T_{a_1}}(\Pi_2):\begin{pmatrix} -1 & 0 & 0 & 0 & 0 & 0 \\ 0 & 1 & 0 & 0 & 0 & 0 \\ 0 & 0 & -1 & 0 & 0 & 0 \\ 0 & 0 & 0 & -1 & 0 & 0 \\ 0 & 0 & 0 & 0 & 1 & 0 \\ 0 & 0 & 0 & 0 & 0 & -1 \end{pmatrix},$$

$$A_{T_{a_2}}(\Pi_2):\begin{pmatrix} -1 & 0 & 0 & 0 & 0 & 0 \\ 0 & -1 & 0 & 0 & 0 & 0 \\ 0 & 0 & 1 & 0 & 0 & 0 \\ 0 & 0 & 0 & -1 & 0 & 0 \\ 0 & 0 & 0 & 0 & -1 & 0 \\ 0 & 0 & 0 & 0 & 0 & 1 \end{pmatrix},$$

$$A_{R_y}(\Pi_2):\begin{pmatrix} 0 & 0 & 1 & 0 & 0 & 0 \\ 0 & -1 & 0 & 0 & 0 & 0 \\ 1 & 0 & 0 & 0 & 0 & 0 \\ 0 & 0 & 0 & 0 & 0 & 1 \\ 0 & 0 & 0 & 0 & -1 & 0 \\ 0 & 0 & 0 & 1 & 0 & 0 \end{pmatrix},$$

$$A_{C_{\pi/3}}(\Pi_2):\begin{pmatrix} 0 & 0 & 0 & 0 & i & 0 \\ 0 & 0 & 0 & 0 & 0 & i \\ 0 & 0 & 0 & 1 & 0 & 0 \\ 0 & i & 0 & 0 & 0 & 0 \\ 0 & 0 & i & 0 & 0 & 0 \\ 1 & 0 & 0 & 0 & 0 & 0 \end{pmatrix}.$$

In the case of $B_S(\Omega_1)$,

$$B_{T_{a_1}}(\Omega_1):\begin{pmatrix} e^{i(2\pi/3)} & 0 \\ 0 & e^{-i(2\pi/3)} \end{pmatrix}, \quad B_{T_{a_2}}(\Omega_1):\begin{pmatrix} e^{i-(2\pi/3)} & 0 \\ 0 & e^{i(2\pi/3)} \end{pmatrix},$$

$$B_{R_y}(\Omega_1):\begin{pmatrix}-1 & 0\\ 0 & -1\end{pmatrix}, \quad B_{C_{\pi/3}}(\Omega_1):\begin{pmatrix}0 & -i\\ i & 0\end{pmatrix}.$$

$$B_{T_{a_1}}(\Omega_2):\begin{pmatrix}1 & 0\\ 0 & 1\end{pmatrix}, \quad B_{T_{a_2}}(\Omega_2):\begin{pmatrix}1 & 0\\ 0 & 1\end{pmatrix},$$

$$B_{R_y}(\Omega_2):\begin{pmatrix}1 & 0\\ 0 & 1\end{pmatrix}, \quad B_{C_{\pi/3}}(\Omega_2):\begin{pmatrix}0 & 1\\ 1 & 0\end{pmatrix}.$$

Similarly for $B_S(\Omega_2)$,

[1] Y. Shimizu, K. Miyagawa, K. Kanoda, M. Maesato, and G. Saito, Phys. Rev. Lett. **91**, 107001 (2003).
[2] M. P. Shores, E. A. Nytko, B. M. Bartlett, and D. G. Nocera, J. Am. Chem. Soc. **127**, 13462 (2005).
[3] Z. Hiroi, M. Hanawa, N. Kobayashi, M. Nohara, H. Takagi, Y. Kato, and M. Takigawa, J. Phys. Soc. Jpn. **70**, 3377 (2001).
[4] Y. Okamoto, M. Nohara, H. Aruga-Katori, and H. Takagi, Phys. Rev. Lett. **99**, 137207 (2007).
[5] M. J. Lawler, A. Paramekanti, Y.-B. Kim, and L. Balents, Phys. Rev. Lett. **101**, 197202 (2008).
[6] Y. Zhou, P. A. Lee, T.-K. Ng, and F.-C. Zhang, Phys. Rev. Lett. **101**, 197201 (2008).
[7] O. Ma and J. B. Marston, Phys. Rev. Lett. **101**, 027204 (2008).
[8] M. B. Hastings, Phys. Rev. B **63**, 014413 (2000).
[9] Y. Ran, M. Hermele, P. A. Lee, and X.-G. Wen, Phys. Rev. Lett. **98**, 117205 (2007).
[10] M. Hermele, Y. Ran, P. A. Lee, and X.-G. Wen, Phys. Rev. B **77**, 224413 (2008).
[11] S. Ryu, O. I. Motrunich, J. Alicea, and M. P. A. Fisher, Phys. Rev. B **75**, 184406 (2007).
[12] J. H. Kim and J. H. Han, Phys. Rev. B **78**, 180410(R) (2008).
[13] F. J. Burnell, S. Chakravarty, and S. L. Sondhi, Phys. Rev. B **79**, 144432 (2009).
[14] J. B. Marston and C. Zeng, J. Appl. Phys. **69**, 5962 (1991).
[15] P. Nikolic and T. Senthil, Phys. Rev. B **68**, 214415 (2003).
[16] R. R. P. Singh and D. A. Huse, Phys. Rev. B **76**, 180407(R) (2007).
[17] R. R. P. Singh and D. A. Huse, Phys. Rev. B **77**, 144415 (2008).
[18] Y.-Z. Zheng, M.-L. Tong, W. Xue, W.-X. Zhang, X.-M. Chen, F. Grandjean, and G. J. Long, Angew. Chem., Int. Ed. **46**, 6076 (2007).
[19] H. Yao and S. A. Kivelson, Phys. Rev. Lett. **99**, 247203 (2007).
[20] A. Rüegg, J. Wen, and G. A. Fiete, arXiv:0911.4722 (unpublished).
[21] J. O. Fjaerestad, arXiv:0811.3789 (unpublished).
[22] N. Read and S. Sachdev, Nucl. Phys. B **316**, 609 (1989).
[23] J. B. Marston and I. Affleck, Phys. Rev. B **39**, 11538 (1989).
[24] I. Affleck and J. B. Marston, Phys. Rev. B **37**, 3774 (1988).
[25] X. G. Wen, F. Wilczek, and A. Zee, Phys. Rev. B **39**, 11413 (1989).
[26] A. M. Polyakov, Nucl. Phys. B **120**, 429 (1977).
[27] M. Hermele, T. Senthil, M. P. A. Fisher, P. A. Lee, N. Nagaosa, and X.-G. Wen, Phys. Rev. B **70**, 214437 (2004).
[28] J. Richter, J. Schulenburg, A. Honecker, and D. Schmalfuss, Phys. Rev. B **70**, 174454 (2004).
[29] G. Misguich and P. Sindzingre, J. Phys.: Condens. Matter **19**, 145202 (2007).
[30] R. Siddharthan and A. Georges, Phys. Rev. B **65**, 014417 (2001).
[31] A. Paramekanti and J. B. Marston, J. Phys.: Condens. Matter **19**, 125215 (2007).
[32] S. Rachel, R. Thomale, M. Fuhringer, P. Schmitteckert, and M. Greiter, Phys. Rev. B **80**, 180420(R) (2009); M. Greiter and S. Rachel, *ibid.* **75**, 184441 (2007); F. F. Assaad, *ibid.* **71**, 075103 (2005).
[33] X.-G. Wen, *Quantum Field theory of Many-Body System: From the Origin of Sound to an Origin of Light and Electrons* (Oxford University Press, Oxford, 2004).
[34] P. Lee, N. Nagaosa, and X.-G. Wen, Rev. Mod. Phys. **78**, 17 (2006).
[35] Y. Ran and X.-G. Wen, arXiv:cond-mat/0609620 (unpublished).
[36] F. Wang, A. Vishwanath, and Y. B. Kim, Phys. Rev. B **76**, 094421 (2007).
[37] D. L. Bergman, C. Wu, and L. Balents, Phys. Rev. B **78**, 125104 (2008).
[38] M. Tinkham, *Group Theory and Quantum Mechanics* (McGraw-Hill, New York, 1964).
[39] K. Sun, H. Yao, E. Fradkin, and S. A. Kivelson, Phys. Rev. Lett. **103**, 046811 (2009).
[40] O. Vafek and K. Yang, Phys. Rev. B **81**, 041401(R) (2010).
[41] K. Sun and E. Fradkin, Phys. Rev. B **78**, 245122 (2008).
[42] X. G. Wen, Phys. Rev. B **65**, 165113 (2002).
[43] F. Wang and A. Vishwanath, Phys. Rev. B **74**, 174423 (2006).
[44] D. S. Rokhsar, Phys. Rev. B **42**, 2526 (1990).
[45] D. M. Ceperley, G. V. Chester, and M. H. Kalos, Phys. Rev. B **16**, 3081 (1977).
[46] P. Horsch and T. A. Kaplan, J. Phys. C **16**, L1203 (1983).
[47] A. V. Chubukov, JETP Lett. **49**, 129 (1989).
[48] S. Sachdev and R. N. Bhatt, Phys. Rev. B **41**, 9323 (1990).
[49] S. Gopalan, T. M. Rice, and M. Sigrist, Phys. Rev. B **49**, 8901 (1994).
[50] V. N. Kotov, O. Sushkov, Z. Weihong, and J. Oitmaa, Phys. Rev. Lett. **80**, 5790 (1998).
[51] O. P. Sushkov and V. N. Kotov, Phys. Rev. Lett. **81**, 1941 (1998).
[52] T. P. Choy and Y. B. Kim, Phys. Rev. B **80**, 064404 (2009).
[53] H. Georgi, *Lie Algebras in Particle Physics* (Perseus Books, Reading, MA, 1999).
[54] S.-S. Lee, P. A. Lee, and T. Senthil, Phys. Rev. Lett. **98**, 067006 (2007).
[55] H. W. J. Blote and R. H. Swendsen, Phys. Rev. Lett. **43**, 799 (1979).
[56] S. J. Knak Jensen and O. G. Mouritsen, Phys. Rev. Lett. **43**, 1736 (1979).
[57] J. Lee and J. M. Kosterlitz, Phys. Rev. B **43**, 1268 (1991).
[58] M. Lee, E.-A. Kim, J. S. Lim, and M. Y. Choi, Phys. Rev. B **69**, 115117 (2004).
[59] B.-J. Yang, Y. B. Kim, J. Yu, and K. Park, Phys. Rev. B **77**, 224424 (2008).
[60] J. J. Sakurai, *Modern Quntum Mechanics* (Addison-Wesley, Reading, MA, 1994).